PhD Thesis

Superconducting joining of Melt Textured YBCO bulks

Bernat Bozzo Closas

2016

Supervised by:
Prof. Xavier Obradors Berenguer
Dr. Xavier Granados García

Tutored by:
Prof. Dolors Baró Mariné

PhD Program in Materials Science
Physics Department – Science Faculty

Xavier Obradors Berenguer, Professor d'Investigació a l'Institut de Ciència de Materials de Barcelona, **Xavier Granados García**, Científic Titular a l'Institut de Ciència de Materials de Barcelona i **Dolors Baró Mariné**, Professora a la Universitat Autònoma de Barcelona

CERTIFIQUEN

Que **Bernat Bozzo Closas**, Llicenciat en Física, ha dut a terme sota la seva direcció el treball que porta per nom "Superconducting Joining of Melt Textured bulk YBCO" i queda recollit en aquesta memòria per optar al Grau de Doctor.

I per a que així consti, signen el present certificat.

Prof. Xavier Obradors Berenguer   Dr. Xavier Granados García   Prof. Dolors Baró Mariné

Llic. Bernat Bozzo Closas

Bellaterra, desembre de 2015

Agraïments

Amb les paraules següents, m'agradaria expressar el meu agraïment a la diversa gent que ha estat rellevant durant la consecució tan de la feina experimental com l'escriptura d'aquesta tesi doctoral. En especial:

Al Professor Xavier Obradors i a la Professora Teresa Puig per donar-me la oportunitat d'entrar en el món de la investigació. Al Doctor Xavier Granados i, altre cop, al Professor Xavier Obradors per la direcció i supervisió d'aquesta Tesi, pel seu recolzament a l'hora de dur a terme el treball experimental associat i per aclarir-me els dubtes que han anat sorgint al llarg d'aquests anys.

A la Doctora Simona Iliescu i Ana Esther pel seu suport durant els primers moments del treball experimental.

A la Doctora Elena Bartolomé per la seva incansable i infinita font d'idees en el camp de la caracterització magnètica de les soldadures.

Als Doctors Miquel Carrera i Jaume Amorós pel desenvolupament del programa "Caragol", eina que ha sigut indispensable per poder extreure informació valuosa de les mesures de magnetització local.

A la Doctora Anna Palau per la seva aportació d'idees en el mètode d'extracció de les densitats de corrent inter- i intra-granular.

Al Professor Pabel Diko i la Doctora Martina Sefcikova per donar-me la oportunitat d'usar el seu excel·lent microscopi òptic, permetent un gran salt qualitatiu en l'estudi de la microestructura de les soldadures.

A tothom que m'ha animat a seguir endavant amb l'escriptura d'aquesta Tesi. En especial als meus familiars pròxims i amics per preguntar-me de tant en tant com ho portava, al Vassil Skumryev per la seva frase "Go home and write your thesis!" i a la Teresa Puig per la conversa que vam tenir, la qual ha estat determinant per acabar de donar la última empenta que faltava per completar l'escriptura d'aquesta Tesi.

A l'Oscar Castaño i a l'Stef Morlens per fer més entretinguda la vida al poble de Hürth (Alemanya) durant les meves dues estades a l'empresa Nexans Superconductors GmbH.

A l'Aitor Lopeandía, Llibertat Abad, Adrián Carretero, Óscar Castaño, Fernando Martínez, Ana Jarana, Patrícia Abellán, César Moreno (i algú més que em dec descuidar, mil disculpes!) per la multitud de sopars al Rinky, excursions diverses i viatges que vam fer junts durant una època de la qual en guardo molts bons records.

A tots els companys amb qui vaig coincidir durant la meva etapa al Departament de Materials Superconductors i Nanoestructuració a Gran Escala de l'ICMAB que no he esmentat

anteriorment. Sens dubte, han estat una gran aportació al meu desenvolupament professional i personal.

A tota la gent de l'ICMAB i ICN2 amb qui comparteixo el dia a dia: Gent d'administració, Manteniment, Servei d'Informàtica, Serveis Científico-Tècnics, estudiants de doctorat i investigadors. Més en pla informal: Al grupet de l'hora d'esmorzar per les sempre interessants i esbojarrades tertúlies i als que fem l'escapada per anar a dinar pels bons moments que passem sota l'arbre prenent el cafè.

Table of contents

Chapter 1.   Preface

1.1   The superconductivity phenomenon

A material is classified as a superconductor when, under a certain temperature, denoted as critical temperature (T_c) two phenomena occur:

(i).   They exhibit null electrical resistance, thus allowing currents to circulate inside the material without dissipating energy.

(ii).   Ideal diamagnetism. If an external field is applied, the material generates a magnetization that fully cancels that external field.
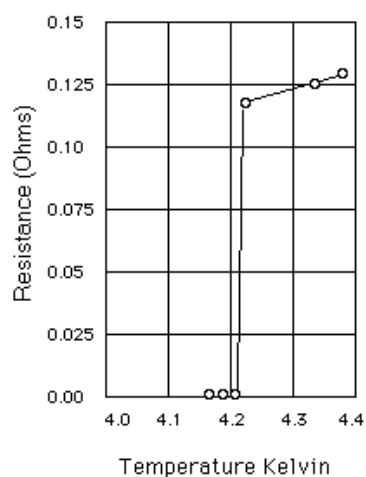
FIGURE 1.1 R(T) CURVE OBTAINED BY **O**NNES DURING HIS STUDY OF THE ELECTRIC BEHAVIOR IN METALS AT LOW TEMPERATURES**,** WHERE THE DRAMATIC DEPRESSION OF THE ELECTRIC RESISTANCE IS SHOWN**.**

The phenomenon of superconductivity was first observed in 1911 by the Dutch scientist Heike Kamerlingh Onnes. Onnes was developing a system able to liquefy Helium and was pretending to study the electrical resistance of several metals at low temperatures. He observed that the electrical resistance of Mercury was suddenly depressed down to zero for the temperatures lower than 4.2K.

On the other hand, a superconducting material exhibits a perfectly diamagnetic behavior. If an external magnetic field *H* is present, the material generates a set of shielding currents that oppose the action of that external field by generating a magnetization *M* that fully cancels the magnetic field *B* inside the material.
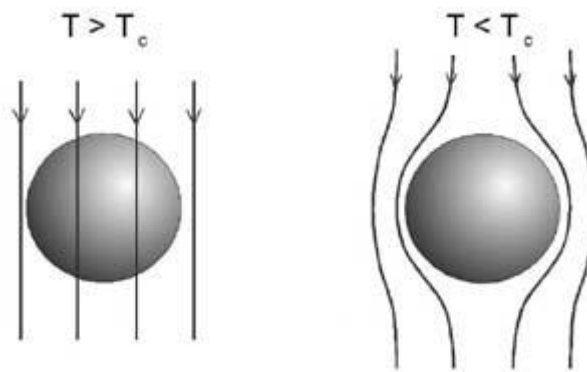
FIGURE 1.2 SCHEMATIC REPRESENTATION OF THE MEISSNER-OCHSENFELD EFFECT, WHERE FOR TEMPERATURES LOWER THAN TC, THE MAGNETIC FIELD IS COMPLETELY EXPELLED FROM THE MATERIAL.

1.2   Theoretical models

Since the discovery of the superconductivity, several theories have been developed in order to explain the origin of this phenomenon. The first developed model was the Two Fluid model in the 1930s by Gorter and Casimir(*1*), which described the coexistence of both normal and superconducting states using a model which assumes the coexistence of two immiscible fluids. Later in 1950, V L Ginzburg and L D Landau developed the Ginzburg-Landau theory which included the case where the superconductivity is non uniform in the material (regions close to magnetic domain boundaries, quantized flux lines, etc.)(*2*)

The details of the development of both theories will not be covered in this preface chapter since the aim of this thesis work is focused in an application of the properties of a particular type of superconductor. However, it is interesting to expose the most relevant aspects of those theories, in particular the physical justification of the existence of vortex lines in a type II superconductor.

1.2.1   Two fluid model and London Equations(1)

The model considers two kinds of electrons: Normal electrons, exhibiting the usual conductivity behavior such as heat dissipation due to the interactions with the crystallographic network; and superelectrons, exhibiting neither heat dissipation nor interactions with the crystallographic network. Those two classes of electrons are described as two different

immiscible fluids, whose density is directly related to the corresponding electron density. Both electron types contribute to the current transport, and the behavior of the material depends on the proportion of each type of electrons, which depends on the temperature. For temperatures higher than T_c, the superelectron density (n_s) is null and, as the temperature is lowered and crosses the T_c value, the superelectron density increases at expenses to the normal electron density.

Before understanding how the perfect conductivity phenomenon is possible, it should be understood the mechanisms that lead to electric resistance. In a metal, only electrons occupying states whose associated velocity is higher than the speed of sound in the material will interact with the phonons in the network. This interaction is known to be the origin of the electrical resistance. Hence, a requirement for a superelectron is that the velocity associated to its state must be lower than the value of speed of sound.

The dissipativeless behavior of superelectrons is, then, possible due to the fact that some electrons occupying states near the Fermi level have been bound in pairs. In each pair, the implicated electron spins are antiparallel, giving a Boson-like behavior and possibiliting that several electron pairs occupy the same state, always with the lowest possible energy and, thus, allowing the electron pairs circulate inside the material without interacting with phonons. The strong overlap between the wavefunctions of each pair implies that the global state of the set of electron pairs will be ordered and cooperative. This means that the individual state for each pair will be the same for all the pairs, and so properties such as center of mass motion or internal orbital state will be. This cooperative behavior also has implications to the binding energy. This binding energy for a single electron pair (denoted as 2Δ) is stronger as the population of superelectrons is increased.

However, this binding energy is weak compared to the order of magnitude of energies related to thermal excitation. For this reason, as the temperature is increased, the population of superelectrons is quickly reduced and not present for temperatures higher than the critical temperature T_c and, furthermore, impossibiliting the existence of superconductivity at room temperature.

In 1935, Fritz and Heinz London described the electrodynamics of the superelectrons in terms of two equations, which were known as London Equations. Both equations describe the two main phenomena involved in superconductivity.

$$\frac{\partial \Lambda \vec{J}_s}{\partial t} = \vec{E}_{eff} \tag{1.1}$$

$$\vec{\nabla} \times \left(\Lambda \vec{J}_s \right) = -\vec{B} \tag{1.2}$$

The Λ value is known as London parameter and has the following expression:

$$\Lambda = \frac{m_e}{n_s e^2} \qquad \text{1.3}$$

The equation (1.1) describes the behavior of the supercurrent under the influence of an electrical field. It implies that, after applying a small pulse of electrical field, a current should remain unaltered in the material as long as there is no other non-null E_{eff} value. This equation describes the persistent nature of the supercurrent.

The second London equation (1.2) describes how the supercurrent behaves in terms of the magnetic field in the material. By applying the Ampere's law to this equation, one reaches to the following expression:

$$\nabla^2 \vec{B} = \frac{\vec{B}}{\lambda_L^2} \qquad \text{1.4}$$

This equation has the form of a screening equation with a characteristic length of λ_L. This characteristic length is known as London penetration depth and it indicates that, in the boundary of a superconducting material, a magnetic field and the supercurrents will be present only in a certain distance inwards the material.

In summary, London equations explain the main characteristics of the supercurrents: In the absence of an effective electrical field, those currents do not decay in time and, when an external magnetic field is applied, the material will generate a loop of screening supercurrents that will prevent that magnetic field penetrate into the material.

1.2.2 Ginzburg-Landau theory and superconducting boundary energy considerations(2)

The Ginzburg-Landau theory is based on the Landau theory for phase transitions. Basically, in the Landau theory for phase transitions demonstrates, by thermodinamical arguments, that when a phase transition occurs, one of the free energy functions is the same for both phases.

Before exposing the details of the Ginzburg-Landau theory, it would be appropriate to summarize the most relevant aspects of the Landau theory applied to the case of a superconductor. Landau classified the phase transitions depending on at which order the derivative of the associated free energy function becomes discontinuous at the phase transition. For instance, one can imagine a phase transition where the volume ($V = -(\partial G/\partial P)_T$) is discontinuous. This phase transition would be classified as first order and this discontinuity would be associated to an internal structure change. In contrast, if the first derivative is continuous, but not second, the phase transition would be classified as second order.

Many phase transitions involve an ordering process and in those cases, an order parameter describing this grade of order can be defined. The superconducting to normal state phase transition is one of those cases and defining an order parameter indicating the amount of electron pairs is appropriate ($n_p = \frac{1}{2} n_s$). For the current case, the use of the Helmholtz free

energy $F(T,n_p)$ is particularly suitable. One can expand this function in terms of the order parameter as follows:

$$F(T,n_p) = F_n + \alpha(T)n_p + \beta(T)n_p^2 + \ldots \qquad \text{1.5}$$

It has to be considered that for $T=T_c$, the order parameter must be zero and that there do not exist metastable states for $T>T_c$. In terms of the behavior of the $F(T,n_p)$ function, it implies that there only exists on minimum and its position determines the value of n_p for each temperature.

Hence, in order to satisfy the requirements exposed above over the $F(T,n_p)$ function, β must be positive and independent to the temperature, whereas α must become negative for $T<T_c$ and positive for $T>T_c$. For temperatures near T_c, the α parameter can be considered to be proportional to $T-T_c$. After applying the condition of minimum, the n_p value in equilibrium can be written in terms of α and β as follows:

$$n_p = \frac{-\alpha}{\beta} \qquad \text{1.6}$$

Landau theory only considered the case for a superconductor with a uniform state. Ginzburg and Landau studied how the free energy would be in the case where the order parameter had a dependence on the position $n_p(r)$. In this theory, a waveform ψ is introduced in the form that it is normalized to n_p.

One can then rewrite the free energy in terms of this waveform and, then, determine the equilibrium state by minimizing this free energy. The details of this mathematic development will not be covered here. Basically, if the free energy function is minimized in terms of spatial changes, one can reach to the following expression:

$$\frac{1}{2m}\left(-i\hbar\vec{\nabla} + 2e\vec{A}\right)^2 \psi + \left(\alpha + \beta\psi^*\psi\right)\psi = 0 \qquad \text{1.7}$$

The equation 1.7 is known as the First Ginzburg-Landau equation and describes de change of the wavefunction respect to spatial changes, at areas close to a superconductor-normal state interface in a non-uniform situation.

By proceeding analogously, but in terms of the magnetic field and, concretely, in terms of the potential vector A, the following expression can be obtained, known as Second Ginzburg-Landau equation:

$$\vec{J}_s = \frac{ie\hbar}{m}\left(\psi^*\vec{\nabla}\psi - \psi\vec{\nabla}\psi^*\right) - \frac{4e^2}{m}\vec{A}\psi^*\psi \qquad \text{1.8}$$

1.2.2.1 Penetration depth and coherence length

From the Ginzburg-Landau theory there can be deduced two characteristic lengths, which are intrinsic to the material. Basically, with some mathematics applied on equation 1.8, expressions analogous to London Equations can be reached. Due to this fact, the existence of a penetration length is also predicted. Furthermore, Ginzburg-Landau theory is also able to determine an expression for λ in terms of α and β, which can be written in the following form:

$$\lambda = \sqrt{\frac{m\beta}{4\mu_0 e^2 |\alpha(T)|}}$$

1.9

From equation 1.7, a second characteristic length can be obtained. This length determines the length where the waveform exhibits significant changes and is named coherence length. The expression for this length is shown in this equation:

$$\xi = \sqrt{\frac{\hbar^2}{2m|\alpha(T)|}}$$

1.10

Note that both expressions exhibit the same α dependence and, thus, the same temperature dependence. The implications of this fact, together with a study of the Normal state-Superconduting state interface energy will allow the definition of a parameter which will be intrinsic to the material and that will let to classify superconducting materials as we will see later.

1.2.2.2 Normal-Superconducing interface energy considerations

It is interesting to consider the case where in the material there coexists both normal state and superconducting state. In particular, the contribution of the normal-superconducting boundary to the free energy will determine the distribution of both normal and superconducting regions.

If the boundary energy is positive, the system will tend to minimize it, leading to large zones of superconducting and normal states. In contrast, if the energy is negative, the system will tend to maximize the surface area by breaking the normal region into a finely divided structure of normal and superconducting regions.

It was pointed out that the sign of the boundary energy depends on the relative magnitude of the λ and ξ lengths. In the regions where a field penetration occurs, the free energy of the system is reduced, whereas if the order parameter is reduced, the free energy is increased.

By considering these two facts about free energy, two extreme cases can be considered:

1. In the case where $\lambda \gg \xi$ the magnetic field will penetrate in a region where the order parameter is not significantly reduced. This implies that the reduction of free energy is much larger than its increase due to the reduction of ψ. Hence, a negative contribution to the free energy, caused by the interface is expected.

2. In contrast, when $\xi \gg \lambda$, the opposite case occurs. The increase of the free energy due to the reduction of the order parameter is more important than the depression caused by field penetration. In consequence, a positive contribution to the free energy is expected due to the existence of a normal-superconducting boundary in this kind of materials.

As it was stated above, both characteristic lengths exhibit the same temperature dependence. It would be convenient to define a parameter that can be used for comparing both characteristic lengths and, at the same time, it is independent to the temperature and, hence, it is intrinsic to the material. By dividing both characteristic lengths in the following form:

$$\kappa = \frac{\lambda(T)}{\xi(T)}$$

1.11

It is trivial to note that this parameter, known as Ginzburg-Landau parameter, will let to classify two types of superconducting materials. Those materials with large κ value will tend to maximize the normal-superconducting boundary, whereas those with small κ values will tend to create large normal and large superconducting zones, in order to minimize the boundary extension.

From the Ginzburg-Landau theory, it can be inferred that for a value of $\kappa = 2^{-1/2}$, the boundary energy is null. Hence, this value of the Ginzburg-Landau parameter can be used as a criterion for classifying the superconductor materials into two categories: Those materials that exhibit values of $\kappa < 2^{-1/2}$ are denoted as type I superconductors and those with $\kappa > 2^{-1/2}$ are denoted as type II superconductors. The boundary energy sign has a huge implication on the magnetic behavior of the material, as it will be explained below.

1.3 Magnetic behavior

The classification of superconducting materials in the two types defined in previous section has implications beyond the sign of the boundary energy. In the case of a normal-superconducing state coexistence in the material, the system will behave differently depending on this sign and, thus, will present different magnetic phase diagrams.

A Type I superconductor presents a single critical field $H_c(T)$, below that, the material is in the superconducting state and exhibits the Meissner-Ochsenfeld effect. For fields of intensity higher than $H_c(T)$, the material is in its normal state (see Figure 1.3a).

The magnetic phase diagram for Type II superconductors is more complex (as schematized in Figure 1.3b). There exist two critical fields: $H_{c1}(T)$ and $H_{c2}(T)$. For magnetic fields of intensities lower than $H_{c1}(T)$, the magnetic field inside the material is completely expelled. For intensities higher than $H_{c2}(T)$, the material is in normal state. The region between the $H_{c1}(T)$ and $H_{c2}(T)$, zones with null and non-null magnetic field coexist. That region in the phase diagram is noted as Mixed State.

As stated in section 1.2.2, the interface energy for Type II superconductors is negative, hence, favoring the formation of that interface. In consequence, the magnetic field is distributed

inside the material in a filamentous form. Those magnetic field threads are known as magnetic vortices.

A vortex is formed by a core, where the ψ wave function vanishes. Obviously, the material is in normal state inside the core, so the magnetic field is not expelled, but concentrated inside the core and spanned for a distance of λ outwards from the core. As deduced from London Equations for a non-simply connected geometry, the magnetic flux crossing the material at the core is quantified in multiples of $hc/2e$. That nucleus is surrounded by a loop of super current whose density is J_s, which ensures the flux quantification and conservation even though the external field is modified(*3*).
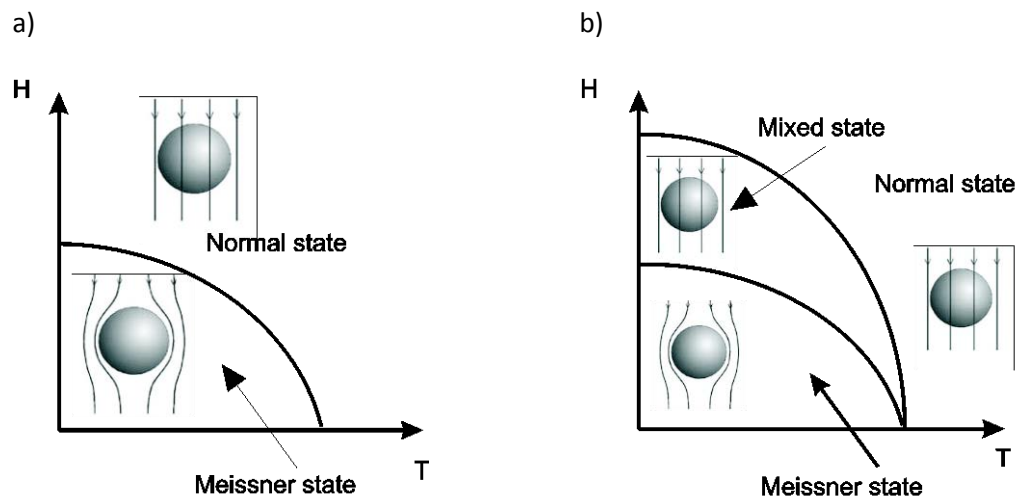
FIGURE 1.3 MAGNETIC PHASE DIAGRAMS FOR (A) TYPE I AND (B) TYPE II SUPERCONDUCTORS.

If the material has some non-superconducting inclusions, such as structural defects or secondary phases, vortices tend to occupy the position of those non-superconducting regions. The superconducting state is less energetic than normal state; hence, in order to destroy this state, a certain amount of energy is necessary. Since the vortex core is in normal state, the presence of a vortex implies an increase of the overall energy of the material. In contrast, when the vortex is situated at the position of a non-superconducting inclusion, no extra energy is needed. For that reason, vortices tend to occupy the position of defects or secondary phases, since the overall energy will be lower. This phenomenon is known as vortex pinning.

The flux pinning phenomenon, together with the persistence of super currents that screen the changes of external flux implies that, when the external field is removed, the material will tend to maintain the flux that crosses it.

It has to be considered that when a transport current is present in a superconductor with vortices present, they are exposed to the Lorentz force:

$$\vec{f}_t = \vec{J} \times \vec{B}$$

1.12

It can be assumed, in principle, that no other forces are present. In this case, vortices will tend to move and, as predicted by the Faraday Law, an effective electric field will be present:

18

$$\vec{E}_{eff} = \vec{v}_{eff} \times \vec{B} \qquad \qquad \textbf{1.13}$$

Hence, the appearance of this effective electric field implies energy dissipation. For that reason, the movement of those flux lines has to be avoided. Commonly, a certain amount of non-superconducting impurities are introduced. Those impurities, together with other type of defects in the microstructure will act as a potential well to the vortices. In consequence, each vortex will be exposed to a Lorentz Force and a pinning force and the presence of impurities and defects will be determinant to the value of the critical current. The more effective the pinning center is, the higher the critical current will be.
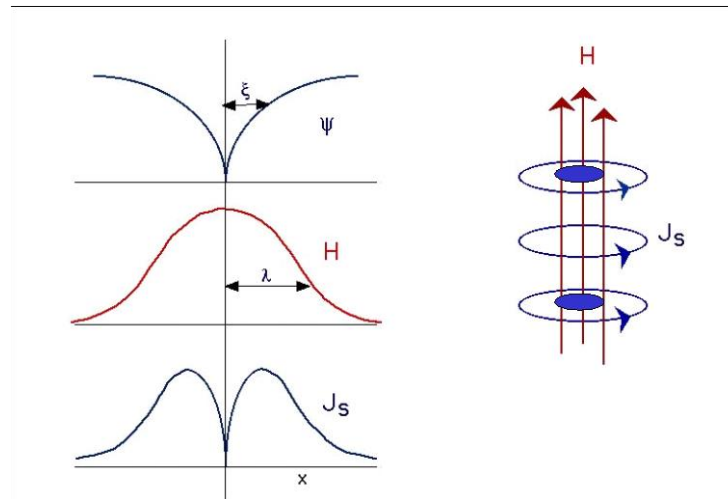
FIGURE 1.4 SCHEMATIC REPRESENTATION OF A VORTEX (RIGHT PANEL) AND EVOLUTION OF THE WAVE FUNCTION, MAGNETIC FIELD AND SHIELDING CURRENT DISTRIBUTION (LEFT PANEL).

1.3.1 Critical state models

As the external magnetic field is increased, shielding current loops appear from the outmost part of the sample. Obviously, the supercurrent intensity cannot overcome the value of J_c. Once it is reached, the zone occupied by supercurrents will grow inwards the specimen. The extreme case, where the supercurrent loops occupy the whole material is known as critical state.

Many authors have investigated theoretically how the response of a type II superconductor would be in a presence of an external magnetic field. It has to be considered that when the critical state is reached and the external field is further increased will tend to reduce the critical current density(*4*). So the aim for many specialists was to establish a dependence between the critical current density and external field that would foresee a *M*(*H*) curve as close to reality as possible.

The field dependencies of several critical state models are summarized with the following expressions:

$$J_c(B) = C \text{ by C.P. Bean(5)} \qquad \qquad \textbf{1.14}$$

$$J_c(B)(B_0 - B) = C \text{ by Y.B. Kim et al.}(6)$$

<div align="right">**1.15**</div>

$$J_c(B)B = C \text{ by J. Silcox}(7)$$

<div align="right">**1.16**</div>

$$J_c(B)B^{-1/2} = C \text{ by K. Yasukochi}(8)$$

<div align="right">**1.17**</div>

$$J_c(B) = C_1 \exp(-B/C_2) + C_3 \text{ by W.A. Fietz et al.}(9)$$

<div align="right">**1.18**</div>

The most fundamental dependence was established by C.P. Bean(5). In this critical state model, the Jc is assumed to be independent to the B field. The model also assumes that the sample is a cylinder whose length is infinite. More details concerning this model will be exposed below, since this model is particularly suitable for the purposes of the current thesis work.

The contribution made by Y.B. Kim et al (6) goes beyond the simple assumption of Bean model and suggests that the J_c(B) can be expanded as power serial. By assuming that high power coefficients are small enough, the serial can be truncated at the linear term, ending to the equation 1.15.

The contribution made by J. Silcox(7) also starts with the same geometric assumptions as the models commented above and then, he introduced the case where the presence of defects of the material is small and, hence, the vortices can move freely. He also considered the interactions between vortices in order to predict the J_c(B) dependence. The result is very alike to the Jc(B) predicted by Kim et al, except for the B_0 constant, as it can be seen in equation 1.16

Finally, both Yasukochi(8) and Fietz(9) found two different empirical equations that suited the magnetic behavior of Nb-Zr superconducting alloys with a form factor of a wire.

1.3.1.1   Bean Model

The most commonly used and the most basic model is known as Bean Model and was first introduced by C.P. Bean in 1962(5, 10). Basically, the model assumes that the current density is constant and independent to the magnetic field. The results predicted for this model are suitable enough for the present thesis work, since the effects of a field dependence will only lead to deformations of the magnetization profile, but will still leave the analysis valid.

The model predicts the magnetization profile for an infinite superconductor cylinder as a response to the variations of the external magnetic field. In Figure 1.5, the *M* profile has been schematized for a complete hysteresis loop.

Assuming that the sample has reached the superconducting state without an external field, when an external magnetic field is applied, immediately the shielding currents will be created near the sample surface. By applying the Bean model, a current ring with a density value of J_c will be present. At the inmost part of the sample, no currents will be present.
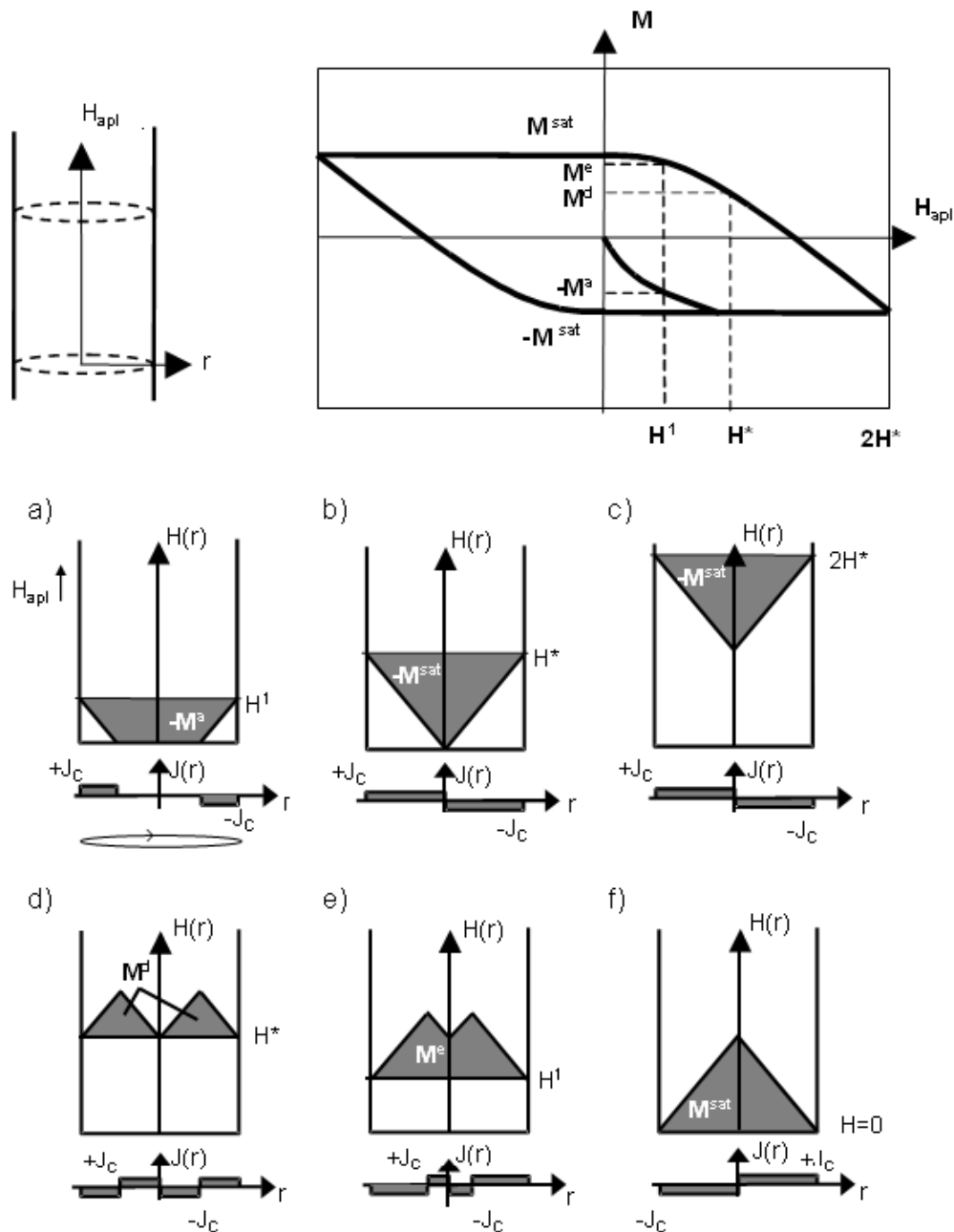
FIGURE 1.5 MAGNETIC HYSTERESIS LOOP FOR AN INFINITE CYLINDRICAL SUPERCONDUCTOR AS PREDICTED BY THE BEAN MODEL (TOP PANEL). MAGNETIZATION PROFILE FOR SEVERAL POINTS OF THE M(H) HYSTERESIS LOOP. (A) AS THE EXTERNAL FIELD IS INCREASED AFTER A ZERO FIELD COOL PROCESS. (B) WHEN FULL PENETRATION IS REACHED. (C) EXTERNAL FIELD IS FURTHER INCREASED UP TO TWICE THE PENETRATION FIELD. (D) EXTERNAL FIELD IS DECREASED BACK TO H*. (E) INTERMEDIATE POINT BETWEEN H* AND H=0. (F) REMNANT MAGNETIZATION.

As the magnetic field is increased, the region with currents present will be wider (Figure 1.5, panel a). The critical state is reached when all the material is filled with currents (Figure 1.5, panel b). The minimum external field value required is called penetration field and it is usually noted as *H**. For more intense external fields, the magnetization remains unchanged, since the sample is saturated (Figure 1.5, panel c).

21

When the external field is, now, decreased, the superconductor will generate superficial shielding super currents, in order to cancel this change. The turn direction of those currents is the contrary respect to those already present. It has to be noticed that the remanence is not maximum if the maximum applied field is lower than $2H^*$, since the current loops created when decreasing the field cannot reach the center and, hence, there still exist the super current loops induced when the sample was first magnetized Figure 1.5, panels d and e). For those applied fields with values higher than $2H^*$, the remanence will be maximum, since the current loops created during the magnetization will be fully cancelled Figure 1.5, panel f).

Chapter 2.   Superconducting materials

2.1   Superconducting materials history

In 1911, the Duch physicist Heike Kamerling Onnes was the first scientist able to liquefy He and, thus, to have the possibility to study the behavior of mater in a range of temperatures not available so far. In this context, many researchers were studying the electrical behavior of metals at low temperatures. Onnes realized that Mercury exhibited an unexpected depression of its electrical resistance for temperatures lower than 4.15K down to unmeasurable values.

In the following years, this phenomenon was also observed in other metals and, later, in alloys and, for each material, the temperature where this depression occurred was determined to be intrinsic. In other chemical elements, the superconductivity also was observed under some conditions of low temperature and high pressure.

Parallely, theorists started searching for models that could explain the phenomenon. Apart from the theoretical models explained in the previous chapter, other theoretical studies predicted a potential presence of superconductivity in organic molecules in 1964. At this time, the models were mature enough to provide a classification of superconducting materials. As explained in chapter 1, according to their magnetic properties, superconductors can be classified into two types: Type I and Type II. Additionally, in 1957, the theorists J Bardeen, L Copper and R Schrieffer developed the theory known as BCS theory that basically explained the phenomenon of superconductivity in the scope of the interactions of electrons in the crystallographic network. However, this theory is based on the fact that the ion activity on the crystal must be rather low, thus limiting the temperatures where superconductivity is possible to those that are lower than 30K.

A significant contribution to the study of the superconductor materials was carried out by J.G. Bednorz and K.A. Muller on 1986(*11*). They produced a ceramic compound that exhibited

superconductivity; this compound was LaBaCuO and exhibited a T_c of 30K. This contribution was important since it was the first non-metal or alloy material to exhibit superconductivity and, furthermore, the first material belonging to a group of superconducting materials where, according to BCS theory, superconductivity cannot occur. This group is known as High Temperature Superconductors.

This fact opened a new investigation line on superconducting materials. On 1987, M.K. Wu and C.W. Chu discovered that by replacing La by Y the critical temperature rose up to 92K(*12*). The resulting compound, $YBa_2Cu_3O_{7-\delta}$ or simply YBCO, is nowadays very commonly used by a large quantity of investors searching for technological applications. The fact that its critical temperature is higher than the nitrogen boiling point (77K) makes this material particularly interesting, since the costs of refrigeration can be severely reduced (in some cases, more than a 10%) if liquid nitrogen is used instead of liquid helium.

Later, other materials based on Copper oxides were studied; nowadays another widely used superconductor is BiSrCaCuO, obtained in several proportions of Bi, Sr and Ca with typical critical temperatures of 108K. This is commonly preferred for fabricating devices for current transport using the powder-in-tube method. Nowadays, the highest Tc known is exhibited by the $HgBa_2Ca_2Cu_3O_{8-\delta}$. Its T_c under pressure is 150K.

In the present work, the superconducting material that will be used will be YBCO due to its promising achievable critical current densities and its high critical temperature; together with its reasonably obtention easiness. Hence, the rest of this chapter is, then, devoted to the explanation of its characteristics and fabrication methods.

2.2 $YBa_2Cu_3O_{7-\delta}$ ceramic material

The $YBa_2Cu_3O_{7-\delta}$ material belongs to the cuprate oxides family of ceramics. All those cuprate oxides have in common it high T_c and layered crystallographic structure and they contain a Cu-O plane, with the CuO_2 stochiometry, normal to the [001] direction (often referred as 'c' axis) that contain mobile charge carriers that are thought to be the origin of the superconductivity phenomenon in those materials.

In particular, $YBa_2Cu_3O_{7-\delta}$ structure is classified as a triple perovskite whose stacking planes are the following: Two BaO planes with a layer of CuO_x chains in between, and two superconducting CuO_2 planes with a Y plane in between (see Figure 2.1).

In general terms, cuprates exhibit a tetragonal or quasi-tetragonal strucuture and, in the concrete case of $YBa_2Cu_3O_{7-\delta}$ compound, this tetragonal structure is distorted to an orthorhombic structure due to the presence of the CuO_x chain layer in its structure. However, at high temperatures, the concentration of O becomes low and their position in the layer become random and the system becomes tetragonal ([100] or 'a' and [010] or 'b' axes have the same cell parameter), whereas for high concentration of O, the oxygen is positioned to form chains with the Cu, thus breaking the tetragonal symmetry and resulting to an orthorhombic unit cell (see Figure 2.2a). As the oxygen content is increased, the 'c' axis size is also affected by shrinking its length (see Figure 2.2b).
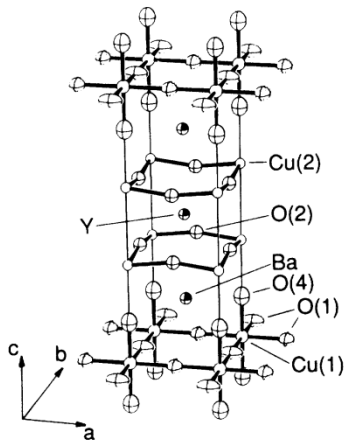
a)   b)
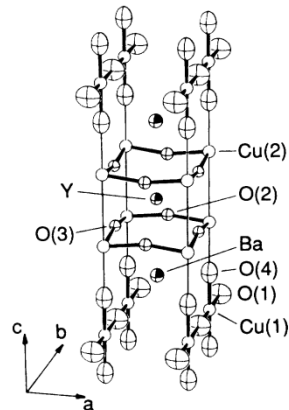
FIGURE 2.1 YBA₂CU₃O₇₋δ UNIT CELLS FOR (A) TETRAGONAL PHASE AND (B) ORTHORHOMBIC PHASE.

This overall change of cell parameters will increase the tensions present in the material. In the case of 'c' axis shrinkage, structure is relaxed by forming series of cracks perpendicular to 'c' axis.
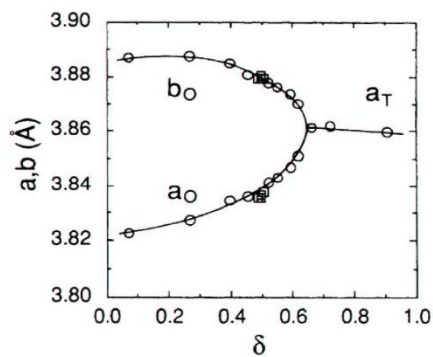
a)   b)
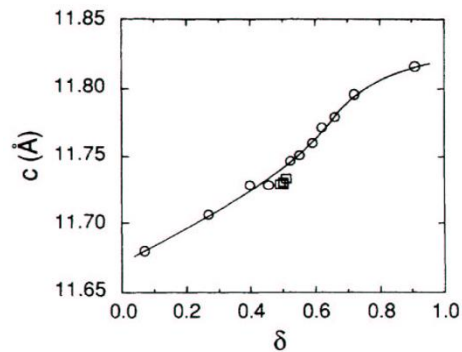
FIGURE 2.2 CELL PARAMETERS, CORRESPONDING TO 'A' AND 'B' AXIS (LEFT PANEL) AND 'C' AXIS (RIGHT PANEL) AS A FUNCTION OF THE OXYGEN CONTENT. A VALUE OF δ=0 INDICATES THAT THE OXYGEN VACANCIES ARE COMPLETELY OCCUPIED, WHEREAS δ=1 MEANS THAT THE STRUCTURE IS OXYGEN DEFICIENT.
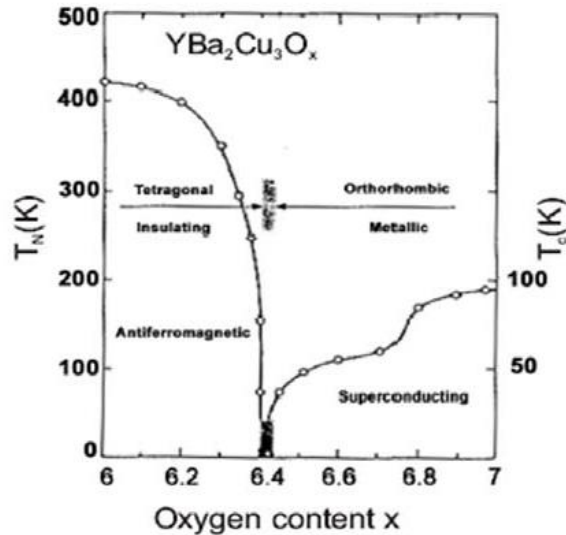
FIGURE 2.3 MAGNETIC AND ELECTRIC BEHAVIOUR OF YBA₂CU₃O₇₋δ COMPOUND AS A FUNCTION OF X=7-δ OXYGEN CONTENT.

The oxygen content not only affects to the structure, but also affects to its electrical and magnetic properties. In Figure 2.3, one can observe the richness of the magnetic and electric behaviour as a function of the oxygen content. For low concentration of oxygen (*x*=6.4), as said above, the material is in its tetragonal phase and becomes anti-ferromagnetic and insulator. Neel temperature evolutes from T_N=420K for *x*=6 down to T_N=0 for *x*=6.4. This oxygen concentration defines the limit between the tetragonal and orthorhombic structure, for higher oxygen content in the structure, the material exhibits superconductivity and its T_c starts increasing from T_c=0 for x=6.4, up to T_c=93K for *x*=7. The electrical properties are also different than those present in tetragonal state, since the material now exhibits metallic behavior.

2.3 Obtention of bulk YBa₂Cu₃O₇₋δ ceramics

As explained above, the superconductivity phenomenon on cuprates mainly occurs in the CuO_2 planes. In particular, supercurrents preferably flow along them. A local distortion on the crystallographic structure, for example a grain boundary, easily blocks the flow of those supercurrents (*13-15*). This blockage can be understood in the way that due to the presence of dislocations at the grain boundary, the local composition of the material at the dislocation is not anymore Y-123 and, hence, not superconductor.

In consequence, the J_c value for a certain material is not intrinsic, but strongly depends on its microstructure. In the framework of potential industrial applications, J_c values of a range from 10^4 to 10^6 A/cm² would be required. For that reason, materials free of grain boundaries and similar defects have to be obtained.

Several techniques can be used for obtaining the YBCO compound. Nowadays, YBCO is mainly fabricated in epitaxially grown thin film form, using either physical techniques (sputtering, pulsed laser deposition, etc.) or chemical approaches such as metalorganic deposition. However, in this Thesis work, the aim is to study a methodology for joining bulk YBCO pieces

so, in consequence, it is worth to explain in detail the most relevant techniques that have historically been used in order to obtain bulk YBCO. Those techniques are exposed below(*16*).

2.3.1 Sintering

Historically, the sintering technique was the first used and also the most simple. This technique is commonly used for the obtention of other ceramic materials. The process consists of a solid state reaction as a first step, which it is carried out as follows:

(i).   Precursors, consisting of Y_2O_3, $BaCO_3$ and CuO powders are carefully milled and mixed.

(ii).   A high temperature treatment is applied in order to cause the solid state reaction and eliminate the carbon from the material. This technique is often referred as calcination.

(iii). The resulting sample is then powdered and milled again, and the process is repeated several times, in order to obtain a fully reacted material.

Once the material has the desired composition, the resulting powder is pressed.

The materials prepared using this technique exhibit T_c values higher than 90K. However, the critical current density does not satisfy the requirements for industrial applications, since those samples exhibit typical J_c values of less than 10 A/cm^2 at zero field and 77K. Those J_c values dramatically decrease when an external field is applied. This poor performance can be understood by the massive presence of grain boundaries in sintered materials. As stated above, those grain boundaries prevent supercurrents from flowing through them, thus reducing the J_c. In order to avoid the formation of grain boundaries other techniques were introduced.

2.3.2 Melt Textured Growth

This technique was first proposed by Jim et al(*17*) and consists of an additional thermal treatment to the pressed pellet, obtained from the sintering technique. This treatment mainly consists of heating the pellet up to a temperature higher than its melting point, followed by a slow cooling in a thermal gradient. Observations on the microstructure reveal that the grains present are highly aligned, thus probably eliminating the weak link presence as indicated in (*16*). The reported J_c for those samples is of the order of 10^4 A/cm^2 at 77K and null field. However, under the presence of an external magnetic field, this J_c is severely depressed, indicating that the flux pinning on those samples is not sufficient.

As an alternative, the inclusion of non-superconducting impurities within the material is a commonly accepted solution for the enhancement of the flux pinning(*16*).

2.3.2.1   Phase diagram

Since YBCO is a ternary compound, the study of the phase diagram is a complex matter. However, the problem can be simplified by considering only a portion of it. In Figure 2.4, the YBCO pseudo-binary phase diagram is presented(*16*). Concretely, the diagram presented consists of a section of the ternary phase diagram along the Y_2O_3, BaO/CuO line.

In this diagram, two congruent solidifications of special interest are present: The phase Y_2BaCuO_5, also known as Y-211, and the phase $YBa_2Cu_3O_{7-\delta}$, often denoted as Y-123.
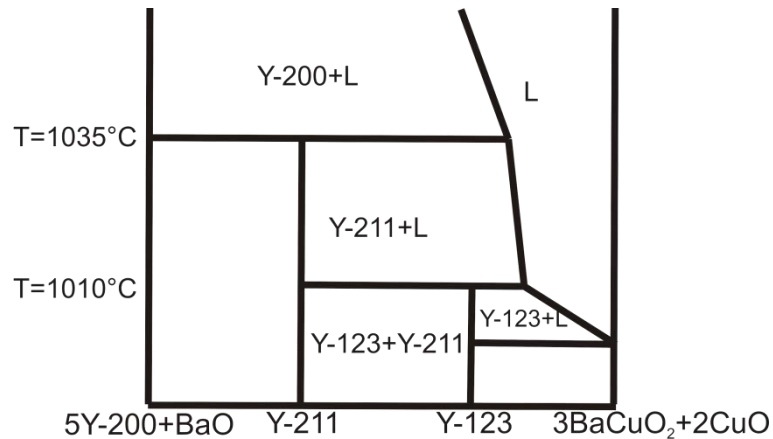
FIGURE 2.4 PSEUDO-BINARY PHASE DIAGRAM FOR THE YBCO MATERIAL ALONG THE $5Y_2O_3+BaO$-$3BaCuO_2+2CuO$ LINE.

At temperatures higher than the melting point at 1035°C, the liquid phase consisting of a mixture of BaO and CuO and the Y_2O_3 solid phase are stable. When the temperature is lowered to values near 1035°C, the liquid phase reacts with the Y_2O_3 phase peritectically, thus forming the Y-211 phase as follows:

$S(Y_2O_3) + L(BaO + CuO) \rightarrow S(Y_2BaCuO_5)$
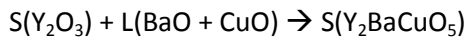
There exists a second pseudo-peritectic reaction at the temperature of approximately 1010°C. In this case, the remaining liquid phase reacts with the Y-211 phase, forming the Y-123 phase, following that reaction:

$S(Y_2BaCuO_5) + L(3BaCuO_2 + 2CuO) \rightarrow S(YBa_2Cu_3O_{7-\delta})$
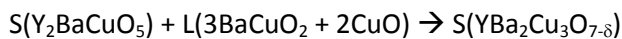
2.3.2.2 Obtention methods

There exist several techniques for generating YBCO textured ceramics using the MTG method. Most of them are variations of the two techniques described below:

2.3.2.2.1 *Bridgman*

The precursors are pressed and bar shaped using an isostatic press. The sample is situated vertically inside the furnace so that a thermal gradient exists along the sample. The temperature profile is that the bar is semi-molten at the zone where the temperature is maxima. The bar is then slowly moved upwards and starts solidifying. In the beginning of the process, the solidified material is polycrystalline. However, due to the fact that under a thermal gradient, the growth rate is dependent to the crystalline orientation, the growth of grains of a certain orientation is promoted at expenses of other orientations. Thus, at the end, an ordered solidification is achieved(*18*).

2.3.2.2.2 *Top seeded melt growth*

In this case, no thermal gradient is applied to the sample, but the slow cooling is carried out by lowering the furnace temperature. The solidification is based on a heterogeneous

solidification. A nucleation center is artificially created by situating a material with similar crystallographic structure and a higher melting point (typically MgO crystals or other RE-BCO single domains, where RE states for rare-earth element, such as Sm or Nd)(*19, 20*). This material is referred as seed and will promote the formation of the solid phase around it respect to other nucleation centers, achieving an ordered solidification. This is currently the most used technique, due to the high quality of the material under the framework of flux pinning and critical current density. In the current thesis work, all the samples used have been obtained by this method(*17*).

2.3.3 Seeded Infiltration Growth (SIG)

Bulk YBCO is known to include several defects such as cracks or voids that weaken the mechanical properties and, usually, are a source of depression of the superconducting properties. Moreover, Top Seeded Melt Growth method is based on the melting of the Y-123 phase and one of the implicit difficulties is the liquid loss that translates to potentially unreacted phases or the shrinkage of the pellet during the thermal treatment.

One of the recent alternatives is the use of Seeded Infiltration Growth (SIG) that basically consists of shaping the pellet with the Y-211 phase. The piece is placed on top of the Y-123 phase that, once melted will infiltrate by capillarity trough the pores present at the Y-211 phase. With the help of a seed, the ordered crystallographic growth can be promoted (*21*).

That method is promising since it is reported to enhance the critical current density (*22*), it can ease the fabrication of pellets with a certain macro-structure such as patterned holes (*23*) and the Y-211 particle size control is improved (*24*).

2.4 Limitations on YBCO single domains

YBCO ceramics obtained by the Top Seeded Melt Growth method exhibit high critical current densities and a satisfactory response to the presence of external magnetic fields.

However, due to the fact that the method is based on a heterogeneous solidification, the quality of the material is severely depressed as the distance to the seed is increased. As the temperature is decreased, other nucleation centers compete with the seed center and other growth fronts are formed.

On the other hand, the solidification of the material starts at the seed zone and advances towards all directions. The texture development will be satisfactory as long as no growing fronts coincide. This situation would occur for pieces with non-simply connected geometries, for example, pieces presenting holes or ring shaped. In those cases, since two growth fronts would collide, a grain boundary or an accumulation of secondary phases would be formed. For both cases, a weak link would be formed.

Those two facts imply a limitation for the geometry and size of textured YBCO pieces. In order to overcome those implicit limitations, several solutions have been proposed.

(i). *Overheating* (*25*). This technique is based on a partial melting of the surfaces of the material, whereas the bulk remains solid. The pieces to be joined are situated in

mechanical contact. The whole setup is submitted under a temperature slightly higher than the Y-123 peritectic point, thus melting only superficially the blocks. The temperature is then slowly lowered in order to ensure a crystallographic reconstruction of the molten zones. This method would allow obtaining larger or more geometrically complex pieces, but it requires a very tight control on the temperature distribution inside the furnace.

(ii). *Multi-seeding* (*26, 27*). Instead of using a single seed, two or more seeds are used in order to promote several simultaneous growing fronts. This technique would allow in principle the obtention of larger YBCO single domains. However, it has to be considered that when two growing fronts meet, secondary phases can be trapped at the coincidence zone. A fine control on the liquid present in the molten sample is required. Furthermore, the situation of the seeds is crucial in order to avoid the formation of grain boundaries, since a bad orientation of the seed would cause a misalignment of the crystallographic axis between the two formed grains.

(iii). *Welding of several single domains, using ReBCO as a welding agent* (*28-32*). This technique is similar to overheating. In this case, a ReBCO system based material (where Re means a rare earth such as Er, Yb or Tm) is used as a welding agent. Those materials exhibit a lower melting temperature than that for YBCO system. Hence, with the appropieate thermal treatment, a localized melting is possible. In the framework of mechanical properties, this method ensures a proper joining of the YBCO pieces. However, the microstructural properties might not be satisfactory, since a high probability of forming non-superconducting secondary phases exists.

Chapter 3.   State of the art and motivation

3.1   Current state of the art

The research on superconductivity has its main interest in using the zero-resistance phenomenon. This fact implies that the final objective in superconductivity is to produce cables made of a particular material.

In the case of YBCO, its production in form of pellets has been successful. However, YBCO is a ceramic material with quite poor mechanical properties. Its brittle nature makes the fabrication of cables impossible.

For that reason, another route was started. Instead of producing bulk YBCO, the route relies on the obtention of YBCO thin films on top of a substrate that has the appropriate mechanical properties (*33-35*). In particular, the possibility of obtaining materials of the form factor of a long tape. This would be particularly suitable for obtaining superconducting cables that would be able to be used for either energy transport or magnetic field generation if they are wounded to form a solenoid.

However, bulk YBCO still have a property that a thin film deposited on a tape cannot beat. Type II superconductors and, in particular, YBCO can trap a high amount of magnetic flux and keep it as long as the material is in superconducting state (*36-38*). This fact still makes bulk YBCO interesting if it is thought as a powerful permanent magnet, especially in the levitation force based applications such as magnetic bearings (*39, 40*).

Since the magnetization value in a type II superconductor depends on the size of the pellet, it is interesting to seek for a method of producing large pellets. However, as exposed before, the existing growth techniques have reached its limit and several joining methods are now under development (*25, 30, 41, 42*).

Recently, a new method has been introduced and it is based on simply using an Ag foil as a welding agent (*10, 43*). This method can now successfully join two single domain YBCO pellets and the welded zone can have a superconducting performance as high as the one of the joined pieces as long as no crystallographic misorientation exists between the two joined tiles.

It has been demonstrated that by adding a certain amount of silver, mechanical properties are improved. Basically, the most relevant aspect of this improvement is a decrease in the amount of cracks present in the microstructure (*32, 44, 45*), mainly since silver is not diffused into the YBCO matrix. Ag forms inclusions inside the matrix instead and, since silver has higher plasticity than YBCO does, those inclusions favor the relaxation of mechanical tensions present at oxygenation time, where the c axis is shrunken. As affirmed in (*46*), the decrease of the concentration of cracks favors the improvement of the critical current density.

Moreover, silver is nowadays being used as an additive for the obtention of bulk Re-BCO pellets of high quality under the scope of superconducting performance, micro-structure characteristics and mechanical properties with high success (*47, 48*).

Therefore, by considering the mutual compatibility of silver and YBCO system in the scope of the superconducting properties, the use of the metal as a welding agent is perfectly feasible (*49*).

3.2 Motivation and objectives

The development of the weld method is partially completed at the start time of this thesis work, but not yet optimized, especially concerning the maximum temperature, and the control of the loss of molten material. Also, the mechanisms that lead to the formation of the weld are unknown and a close look to the YBCO-Ag phase diagram should be carried out with the help of a deep study of the microstructure at the weld zone. The welding method should be extended to include crystallographic misorientations, so the implications of such misorientation on both microstructure and the electromagnetic properties should be carefully studied.

The Ag-assisted welding method is a promising workaround for overcoming the limits of the Top Seeded Melt Growth technique. The feasibility of the use of this welding method has to be determined and the information obtained from the work detailed in this manuscript will be crucial for this determination.

Hence, this thesis work is focused in the following aspects:

(i).   The refinement of the welding methodology for YBCO pellets in order to solve the issues present at the time this thesis work was started.

(ii).   Characterization of the microstructure of welded pellets. This will be crucial in order to predict a model that would explain how the weld is formed during the thermal treatment.

(iii).   To develop a suitable quantitative analysis tool for evaluating the weld quality in terms of its superconducting behavior. This will be carried out by locally analyzing the current density patterns obtained from Hall Probe microscopy.

(iv).   The expansion of the methodology to include welds with crystallographic misorientation and study the influence of such a crystallographic misorientation on the electric and magnetic properties. It is expected that the weld quality will be affected by this misorientation and it is particularly interesting to be able to determine the limits of the methodology under the point of view of potential industrial applications.

3.3   Publications summary

The main goal of this work is to explore the limits of the welding technology. At the initial stages of it, the weld methodology was under optimization. In particular, a suitable welding agent and thermal treatment was not yet fully determined. The first published work explains how an appropriate Ag foil thickness is determinant in order to properly obtain a high quality weld (see section 4.1).

In parallel, a Hall Probe microscope was being developed in order to obtain local magnetization maps from the welded samples. This was going to be the primary experimental setup used for the magnetic properties characterization of the welds. All the studies carried out on the critical current density distribution strongly depend on the data collected from this setup. Details will be introduced in section 6.1.

The critical current density distribution for the case of two welded single domains is quite complex and its study requires a previous simulation of this distribution. That simulation was done by using a specially made software that simulated the critical current density for several ideal superconducting geometries containing several non-superconducting inclusions in its working space. One particular example was the simulation of welded samples. The weld was simulated as an alternating pattern of superconducting and non-superconducting zones. The work is summarized in section 6.2

The knowledge acquired from the simulations was used for the real critical current density maps obtained from the Hall Probe microscopy measurements. In particular, from those maps, two important critical current density values were extracted: That for the single domain, known as intra-granular critical current density and that for the welded zone, known as inter-granular critical current density. The ratio between those two values was used as a figure of merit for evaluating the quality of the weld. This figure of merit was later used when the welding methodology was extended to contain the case were the welded single domains had a mutual crystallographic misorientation.

The case of disoriented welded single domains is particularly interesting if the welding method is though for a way to produce large superconducting magnets, where several single domains should be joined and, for field geometry purposes, a crystallographic misorientation must exist between the welded tiles.

With the extension of the weld methodology to the case of disoriented welds, the interest of studying the microstructure and the mechanical properties arose. The study of the microstructure would help to understand some still open questions about the weld formation, specially focused on predicting the mechanisms that lead to the weld zone melting and posterior recrystallization.

Of course, the weld should exhibit reasonably good mechanical properties, at least comparable to those present in the starting material. Several welded samples with different misorientation angle were chosen to perform nano-indentation tests. Basically, the technique consists of applying some force on the material using a sharp tip. This causes a local deformation of the material and its shape can be later analyzed in a Scanning Electron Microscope. In this case, indentation was performed at several zones far from the weld in order to record the mechanical properties of the starting material and then, indentation was performed at the weld zone. The results were then compared to those obtained from the magnetic measurements.

In next chapters, those works will be situated and introduced in their appropriate context in the subject. Each section that refers to a certain supporting publication will be labeled with the word "WORK". The section will contain a brief introduction, justification and result discussion. The publications will be included at the end of each chapter, after the summary section.

The following table indicates where each publication is situated:

Chapter 4	**WORK 1:** Melting of Ag-YBa$_2$Cu$_3$O$_7$ interfaces: the path to large area critical current welds
	WORK 2: Oxygenation Thermogravimetry of TSMG YBCO Bulk Superconductor
	WORK 3: Obtention and characterization of YBCO/Ag/YBCO welds at different misorientation angles
Chapter 5	**WORK 4:** Influence of crystal plane on the welding quality of YBCO bulk superconductor
Chapter 6	**WORK 5:** In-field magnetic Hall Probe microscopy studies on YBa$_2$Cu$_3$O$_7$ based superconductors
	WORK 6: Simulation of dc magnetic effects due to geometrically defined grain boundaries in type-II superconductors
	WORK 7: Determination of the inter- and intra-granular critical currents in superconducting YBa$_2$Cu$_3$O$_7$ welds
	WORK 8: Vortex pinning regimes in YBa$_2$Cu$_3$O$_{7-x}$ bulk boundaries investigated by quantitative magnetic Hall microscopy
	WORK 9: Effective silver assisted welding of YBCO blocks: mechanical versus electrical properties

Chapter 4.   Obtention of YBCO/Ag/YBCO welds

The use of welding techniques is a promising method for overcoming the limitations of the several existing growth methods. The choice of an appropriate welding agent is crucial for the success of the weld method.

So far, several attempts were made using ReBCO superconductors (Re states for rare-earth element) exhibiting lower melting temperature than that for YBCO. The main idea is to provoke a local melting of the zone to be joined in order to later reconstruct the crystallographic structure at the molten zone. However, the cell parameter of the welding agent is slightly different from that of YBCO, thus creating undesirable lattice mismatches that would degrade the superconducting performance at the ReBCO/YBCO interface.

Another approximation is the use of Ag-YBCO composites. This composite has a melting point in air of 980°C, instead of the 1010°C for the YBCO alone. The problem of the lattice mismatch is eliminated and a high quality weld is expected to be obtained.

The process can be further simplified by using a silver foil as a welding agent instead.

The thermal treatment consists of heating the sample up to a temperature higher than the melting point of the welding agent, but lower than that for the YBCO. A slow cooling is then performed in order to promote a crystallographic reconstruction of the molten zone. The choice of the maximum temperature, dwelling times and cooling ramps depend on the chosen welding agent.

4.1 WORK 1: Melting of Ag-YBa2Cu3O7 interfaces: the path to large area critical current welds

In this work, the influence of the silver foil thickness was investigated. Silver foils with a thickness of 25μm and 50μm have been used with two orientations (silver plane parallel and perpendicular to "c" axis).

In order to investigate the shape and dimensions of the molten zone, the thermal treatment was interrupted before the slow cooling part and the sample was quickly cooled down from the maximum temperature in order to create a polycrystalline reconstruction of this molten zone. With that analysis, it was intended to understand the Ag diffusion dynamics during the thermal treatment. In particular, the measurement of the width of the molten zone is an indication of the distance the Ag has diffused into the YBCO matrix. The Ag penetration depth can be controlled by the thickness of the Ag foil used.

Besides the study of the molten zone morphology, the influence of the presence of cracks on the pieces to be joined was also analyzed. Cracks perpendicular to the plane formed by the weld zone were observed to be the source of undesired Ag rich liquid loss, since this liquid exhibits a very low viscosity and easily moves along the surfaces due to capillary effect. This fact is further proven in the analysis carried out on the movies obtained from the in-situ observation of the thermal process.

In spite of the potential issues on the distribution of the liquid phases during the thermal treatment, once the maximum temperature, cooling rate, and slow cooling temperature window are correctly tuned, the molten zone is successfully reconstructed and it preserves the superconducting performance of the sibling joined pieces. The reconstructed zone is free from inclusions of solidified Ba-Cu-O or Ag rich liquids. However, a variation of the Y-211 particle distribution is observed. Specifically, a tendency to form larger particles than those present in the rest of the YBCO matrix is observed. The high quality of the weld is proven by Hall probe magnetic imaging measurements. The details of the nature of those measurements and their associated analysis tools will be later discussed.

4.2 In-situ observation of the thermal treatment

In order to further study the phenomena involved in the thermal process, a special furnace equipped with a video-camera was built. In one of the obtained movies, the presence of a low viscosity liquid was detected during the thermal treatment. In Figure 4.1 it can be observed that several clearer zones exist. Those clearer zones change in position. The presence of 'c' cracks (cracks parallel to a (001) plane) and due to the fact that the Ag foil is perpendicular to those cracks, it is highly probable that those promote the liquid migration by capillarity effect.
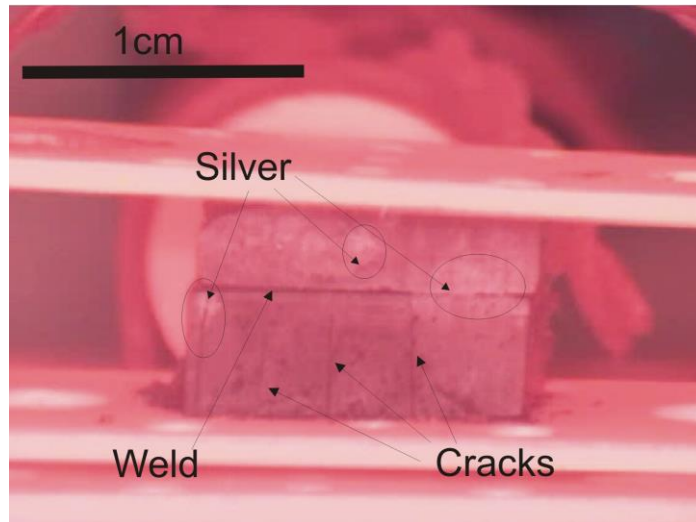
Liquid loss is an issue for the correct formation of the weld, since an uncontrolled migration of Ba-Cu liquid could cause the formation of undesired secondary phases or, even, void zones at the weld. In Figure 4.2, four slides extracted from another movie show that as the thermal treatment advances, a black stain grows at the top and bottom alumina plates that hold the YBCO/Ag/YBCO sandwitch.
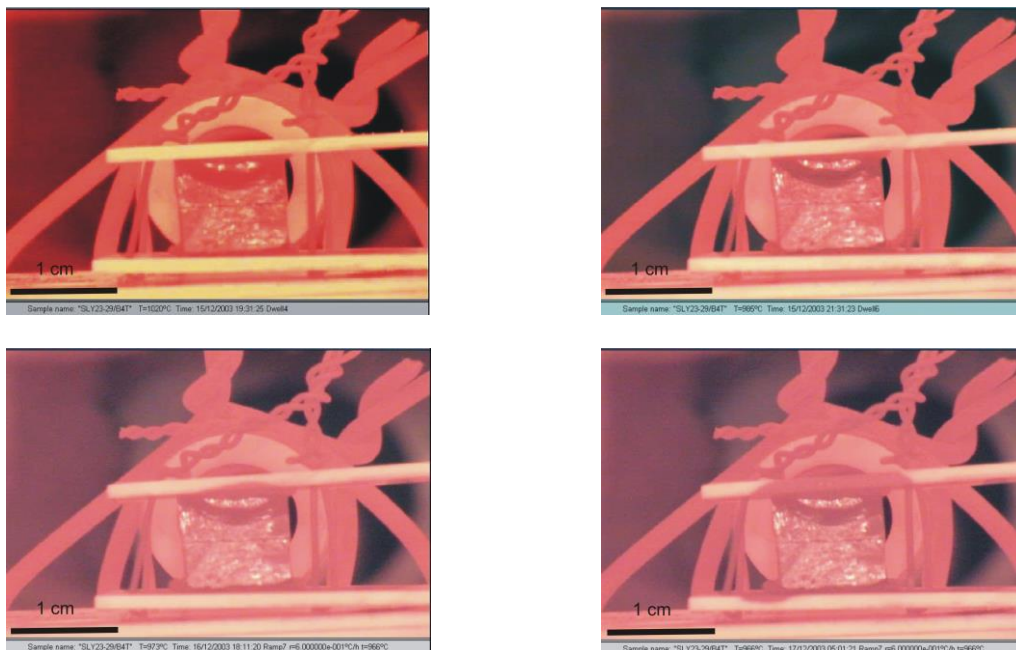
That stain appearance was correlated to a significant mass loss between the beginning and the end of the treatment. It was postulated that the alumina holder could have some porosity that would promote that liquid migration. This liquid was analyzed using EDX and it was determined to contain a high quantity of Ba and Cu (see Figure 4.3).
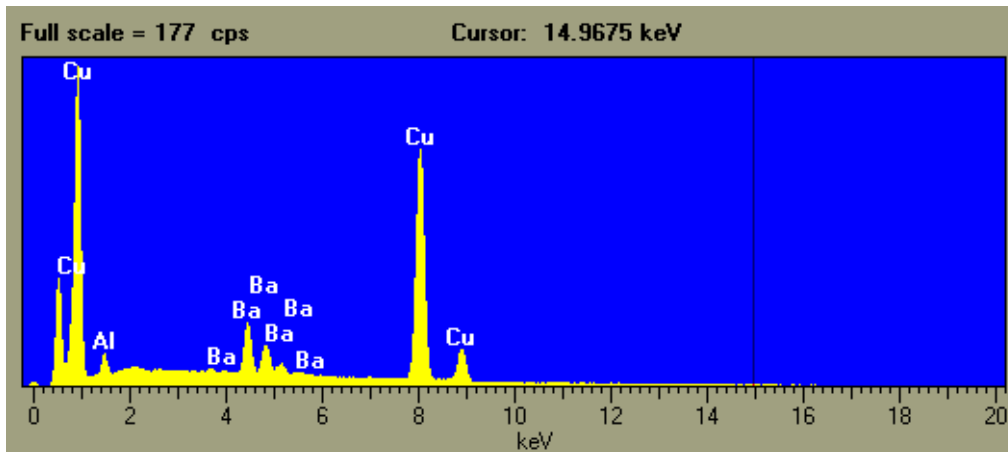
FIGURE 4.3 EDX SPECTRA FROM THE ALUMINA SAMPLE HOLDER. THE BA AND CU PEAKS ARE CLEARLY DISTINGHISHED, INDICATING THE NATURE OF THE SOLIDIFIED LIQUID

In spite of the potential issues on the distribution of the liquid phases during the thermal treatment, once the maximum temperature, cooling rate, and slow cooling temperature window are correctly tuned, the molten zone is successfully reconstructed and it preserves the superconducting performance of the sibling joined pieces. The reconstructed zone is free from inclusions of solidified Ba-Cu-O or Ag rich liquids. However, a variation on the Y-211 particle distribution is observed. Concretely, a tendency to form larger particles than those present in the rest of the YBCO matrix is observed. The high quality of the weld is proven by Hall probe magnetic imaging measurements. The details of the nature of those measurements and their associated analysis tools will be later discussed.

4.3   Liquid loss control

The information obtained from the in-situ movies in the previous section indicates that during the process, an important quantity of liquid is expelled from the sample and remains placed onto the sample holder. The mass measurements on the sample before and after the thermal treatment, compared to those measured on the sample holder confirm this fact.

That liquid loss could be favored in part by the nature of the Silver rich liquid and the liquid rich of Barium and Copper both observed in section 4.2. The second video proves that the silver rich liquid exhibits a very low surface tension, favoring its transport out from the welding zone. This transport phenomena might also be enhanced by a reaction between the YBCO material and the alumina sample holder.

That liquid loss has to be controlled, since a massive migration of the molten liquid could imply a defective formation of the weld. For that reason, the relation between the mass loss related to liquid loss and the several preparation conditions will be studied. Concretely, the maximum temperature, the amount of silver used and the effect of modifying the sample holder will be considered. The mass loss for all the cases has been normalized to the weld surface, since the phenomena involved in the formation of the weld is quasi-superficial

4.3.1 Influence of the T_{max} parameter

In principle, one would expect that the higher the T_{max} is, the more important the liquid migration becomes. For that, reason, several T_{max} temperatures have been tested.

In Figure 4.4, the mass loss evaluated for a range of T_{max} is presented. It can be appreciate that the relative mass loss is more evident for higher T_{max}. It is also important to note that for each tested T_{max}, there exists a wide range of $\Delta m/S$ values. This indicates that the loss of liquid is controlled by T_{max}, but this parameter is not the only one that influences on the quantity of expelled liquid. So, more parameters have to be investigated.
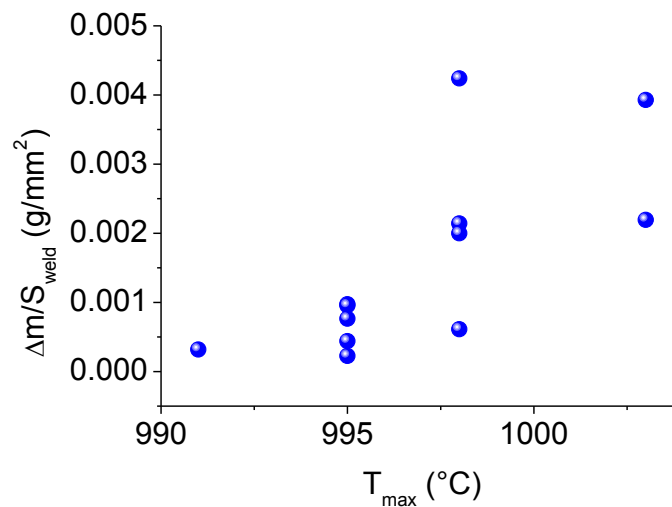
FIGURE 4.4 INFLUENCE OF THE MAXIMUM TEMPERATURE ON THE MASS LOSS

4.3.2 Influence of the silver foil mass

The second parameter investigated is the quantity of the silver used. In that framework, the relative mass loss has been compared to the silver foil mass. The aim for this study is to determine whether the quantity of silver used will regulate the quantity of lost liquid.

It can be appreciated in Figure 4.5, that the data points are randomly dispersed. This indicates that the quantity of silver used has no evident influence on the $\Delta m/S$ value.
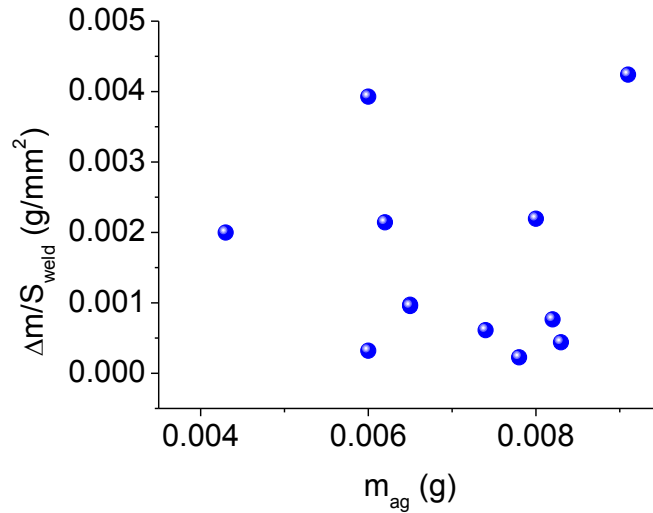
FIGURE 4.5 INFLUENCE OF THE SILVER FOIL MASS ON THE MASS LOSS

4.3.3 Influence of the sample holder material

In the former sections, it has been introduced that the mass loss cannot be easily controlled by changing the preparation conditions. It must be considered that the alumina sample holders used, exhibit some porosity that might favour the migration of liquid. In order to avoid this capillarity effect, two MgO plates have been introduced between the alumina holders and the sample. It has been reported that a presence of Mg in the crystallographic structure of the YBCO material dramatically decreases the T_c(50, 51). This T_c depression has been observed in the cases when Mg has been present in the precursors. However, in the present situation, the MgO plates are only in contact with the external surfaces of the sample and those surfaces are parallel to the weld plane. Due to the fact that the temperatures used are below the peritectic point of Y-123 phase and below the melting point of the MgO material, the only mechanism that would case Mg to penetrate into the YBCO structure is a solid state diffusion. Since, the solid state diffusion is a very slow phenomenon; it is only expected to find Mg only in a superficial layer. Hence, it is not expected to degrade the superconducting properties by using MgO plates.

In Figure 4.6, it has been plotted the relative mass loss for several welded samples, before and after introducing the MgO plates. For the alumina only samples, the mass loss was uncontrolled and, as explained in former sections, its relation with the preparation conditions was not trivial. For the alumina with MgO welded samples, the mass loss becomes a controlled and almost null value.

By introducing the MgO plates, the expelled liquid is no longer in contact with the alumina material, so one of the mechanisms that favored the liquid migration has completely been mitigated. It is important to note that with that modification of the sample holder, the possible problems related to an excessive liquid migration can now be avoided.
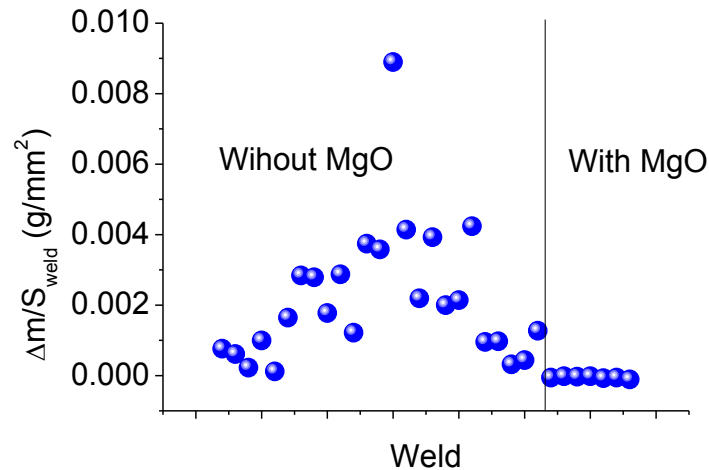
FIGURE 4.6 INFLUENCE OF THE MODIFICATION OF THE SAMPLE HOLDER ON THE MASS LOSS

4.4 WORK 2: Oxygenation Thermogravimetry of TSMG YBCO Bulk Superconductor

Y-123 system has two stable crystallographic phases, the tetragonal phase and the orthorhombic phase. The change between each other is governed by the oxygen content at the unit cell. The orthorhombic phase is the only phase interesting in the scope of the current thesis work, since when Y-123 unit cell is orthorhombic, superconductivity occurs.

Since the growth of Y-123 involves the use of high temperatures, the oxygen content of the Y-123 system as grown is deficient in oxygen content; hence the material is not exhibiting superconductivity.

So, in order to incorporate oxygen into the crystallographic structure an additional thermal treatment has to be applied to the material. Typically the thermal treatment consists of heating the sample up to 450°C for several hours in an oxygen rich atmosphere. The amount of time needed to fully oxygenate the sample depends on its size and shape.

The phase shift involves a change on the cell parameters between both phases, in concrete, 'c' axis shrinks by 0.12A, 'a' and 'b' axes slightly change their parameter by about 0.02A (growth of 0.02A for the 'b' axis and a shrinkage of 0.02A for the 'a' axis). This fact creates a tensile stress between the 'ab' planes and a more complex scenario of both tensile and compressible stress at the 'ab' plane itself.

That collection of stresses present is known to be the origin of the crack formation at the YBCO material during the oxygenation process.

The development of cracks is known to shorten the time needed for fully oxygenating the YBCO pellet. For instance, if a pellet of 3.5mm is considered, by applying the continuity equation for oxygen deficiency would result in a needed time of 122 days, much longer than the reported required time for a bulk YBCO of that size.

In this work, the change of mass during the oxygenation process was measured by using thermogravimetric techniques. A better understanding about the role of the crack formation on the oxygenation time is pretended in this work.

The starting material was a virgin tetragonal YBCO pellet that was heated up to 450°C and held at that temperature until the mass change became null. Following that, the sample was heated up to 900°C first in oxygen rich atmosphere and then changed to argon atmosphere in order to restore the tetragonal state. Temperature was lowered to 450°C and the oxygenation process was repeated. A second heat-cool sequence was done in order to record a third oxygenation for comparison with the former two.

The first oxygenation curve reveals a significant shortened oxygenation time than that theoretically predicted for a single crystal that has the size of the sample used. This fact would indicate that as oxygen starts penetrating the material, the stress produced by the cell parameter change already starts to create cracks at the oxygenated portion. Once cracks are formed, oxygen can penetrate more easily into the material, since the contact surface between the material and the environment is dramatically increased. Second and third oxygenation curves show a required oxygenation time that it is significantly shorter, mainly due to the fact that the cracks are already present before starting the oxygenation process.

Once cracks are formed, if their spacing is considered and the continuity equation is applied to this scenario, the requested time predicted is in agreement with the experimental results extracted from the thermogravimetric measurements.

4.5 WORK 3: Obtention and characterization of YBCO/Ag/YBCO welds at different misorientation angles

Since the introduction of the Top Seeded Melt Growth method for the obtention of bulk YBCO single domains, many investigators have searched for several solutions in order to overcome the implicit limitations involved in this methodology. One of the most successful methods consisted in using a silver assisted welding method. The method is successful in joining two YBCO pieces, yet preserving the superconducting performance at the joined zone as long as both YBCO pieces had no mutual crystallographic misorientation.

However, for technological applications, it has to be considered the case where the two joined single domains do not share the same crystallographic orientation. This case applies, for example, to superconducting bearings, where the magnetic field should exhibit a radial geometry or a flywheel where the magnetic field should be geometrically axial.

Super currents preferably flow in (001) plane (also known as 'ab' planes). In order to obtain the maximum performance from the superconducting component, the magnetic field should remain as perpendicular as possible to those ab planes. In order to achieve this condition, the joining of several single domain YBCO pieces with crystallographic misorientation is required.

Having in mind technological applications such as flywheels or magnetic bearings, one realizes that a crystallographic misorientation between the joined tiles should be introduced.

For the case of the YBCO parallelepiped-like crystallographic structure and for a joint perpendicular to the ab plane, three canonical misorientations can be introduced:

- By rotating the 'ab' planes, leaving the c axis unchanged. This is known as [001]-tilt.
- By rotating around the axis parallel to the joint. This is known as [100]-tilt.
- By rotating around the axis perpendicular to the joint. This is known as [100]-twist.

The choice of the appropriate misorientation depends on the case of the geometry needed and its relationship with the magnetic field being applied, in order to optimize the magnetic performance of the material, the field lines must be parallel to the 'c' axis. This fact makes one or other type of misorientation preferable in front of the others.

For example, a flywheel consists of a superconducting wheel on top of a permanent magnet wheel. In this case, the magnetic field lines are locally perpendicular to the wheel, thus requiring the 'c' axis to be perpendicular to the wheel as well, so, in consequence, the [001]-tilt misorientation would be the optimal in this case.

In contrast, in a motor, the magnetic field lines have a radial geometry. Therefore, for an YBCO bearing, the 'c' axis should also be radial, thus making the [100]-tilt misorientation the desirable one.

In this thesis work, the first case has been considered and all the samples used for the experimental work have been welded using the [001]-tilt type of misorientation. The main reason for choosing this case is that all the tools used so far to characterize the magnetic performance of the welds can still be used. Moreover, the [100]-tilt would require a more complex magnetic field generation in order to be able to simultaneously magnetize both joined tiles perpendicularly to their 'c' axis, in contrast to the [001]-tilt, where a simple longitudinal coil or a set of Helmholtz coils can be used to generate the desired magnetic field geometry.

For the chosen [001]-tilt type misorientation, one can consider two cases: To rotate only one of the tiles a certain angle θ, or to introduce the same misorientation by rotating both tiles an angle of $\theta/2$, both cases have been considered.
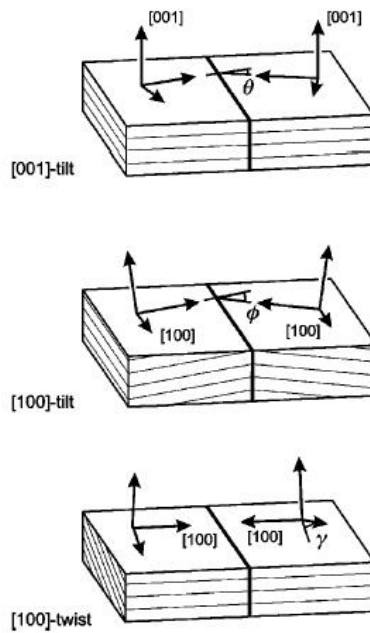
In order to introduce the desired misorientation, samples were cut using the schema illustrated in Figure 4.8. Several misorientations were considered: 0 deg, 5 deg, 10 deg, 15 deg, 20 deg for both symmetrical and asymmetrical cases. Despite this discrete distribution of misorientations, certain discrepancy of the desired misorientation value and the actual value was expected due to the limitations of the cutting facilities used, leading to a more continuous distribution of misorientations.

Since the twin planes present in the ab plane are an indication of the [100] and [010] crystallographic axes, the mutual misorientation of those twin planes at each side of the weld was measured. The obtained angle was considered to be the real misorientation angle.

The necessary microstructural observation involved in this angle determination also allowed characterizing the joined zone shape. That weld zone exhibits a non-linear shape in spite the faces to join were completely flat. This fact indicates that this non-straight structure was formed during the recrystallization process. A more complete microstructural study on those disoriented welded samples is discussed later in Chapter 5.

For each misorientation the figure of merit, consisting of a ratio between the intra- and inter-granular critical current density (J_c^{GB}/J_c^{G}) was determined, in order to obtain its angular dependence (the details about how to obtain this ratio will be later discussed in section 6.3). A depression of this figure of merit was expected since a grain boundary is created. Since the measured depression was lower than that expected, the obtained angular dependence was compared to those obtained in similar works for both thin film and bulk cases, showing that the case of welded samples was similar to that determined from other studies about grain boundaries on bulk YBCO.

More precisely, the smaller angular dependence of bulk case, as compared to the thin-film case clearly indicates a modified behavior: Thin-film case clearly shows a higher angular dependence of the J_c^{GB} than that for bulk cases. The scenario is radically different at high angles, where both dependencies tend to merge. The origin of those different behaviors could be different vortex pinning regimes that change depending on the nature of the sample (thin-film or bulk) and the nature of the grain boundary (high angle or low angle).

For that reason, a more thorough study on the magnetic behavior of the disoriented welded samples was performed. That study included the analysis of the field dependence of Hall probe image. The details of this work are later discussed in section 6.4.

4.6   Summary

In order to obtain successfully welded pellets, several preparation parameters were tuned, such as silver foil thickness, thermal treatment temperatures (T_{max} and slow cooling window temperatures) using the microstructure and magnetization maps as a feedback for the test of the success of the use of a particular set of parameters.

The development of a furnace equipped with an in-situ observation system provided very useful information about the thermal process. In particular, some movies recorded with this system revealed the existence of a very low viscosity liquid that was moving quite easily along the surfaces of the material (cracks and external surface). The same setup revealed a potential drawback of the welding technique consisting of an evidence of liquid loss.

That liquid loss was studied as a function of the thermal treatment parameters, revealing no relation at all with any of the studied ones (maximum temperature and silver foil mass). The amount of lost liquid was, then, governed by nature of the sample holder used. The introduction of a MgO plate as a barrier between the alumina holder and the sample stopped the liquid loss.

The oxygenation process was known to be the origin of the crack formation. So, the change of mass related to the oxygen gain during the annealing process was measured using

thermogravimetry. With the careful study of the thermogravimetric curves, an agreement between the calculated oxygenation times predicted by the diffusion equations and the experimental results was found if the experimentally measured crack separation was taken into account.

Finally, once the thermal treatment conditions were satisfactorily tuned, the method was extended to include a crystallographic misorientation between the joined tiles. The impact of this crystallographic misorientation on the magnetic properties was studied. The details of the study will later be discussed.

WORK 1:

"Melting of Ag– $YBa_2Cu_3O_7$: The path to large area high critical current welds"

S. Iliescu, A. E. Carrillo, E. Bartolomé, X. Granados, B. Bozzo, T. Puig, X. Obradors, I. García and H. Walter

Supercond. Sci. Technol. **18** (2005) S168–S172

DOI: 10.1088/0953-2048/18/2/034

WORK 2:

"Oxygenation Thermogravimetry of TSMG YBCO Bulk Superconductor"

P Diko, X Granados, B Bozzo and P Kulík

IEEE Transactions On Applied Superconductivity. **17 Issue 2** (2007) 2961-2964

DOI: 10.1109/TASC.2007.898219

WORK 3:

"Obtention and characterization of YBCO/Ag/YBCO welds at different misorientation angles"

B Bozzo, E Bartolomé, X Granados, T Puig and X Obradors

Journal of Physics: Conference Series **43** (2006) 401–404

DOI: 10.1088/1742-6596/43/1/100

Chapter 5.   Microstructural characterization

A proper study of the microstructure of the welded YBCO pellets is crucial in order to understand the mechanisms that allow the formation of the weld and, at the same time, it provides information about the success or failure of its formation. The study presented in this chapter is based on the pictures obtained from both optical microscope and Scanning Electron Microscope (SEM).

A basic microstructural characterization has been systematically carried out in all welded samples. It consists of a sequence of pictures obtained from the optical microscope with polarized light. The aim of this basic characterization was to check whether the weld has been successfully formed or not. In previous works, this basic characterization also gave useful information about the level of optimization of the thermal process (*10*).

The Scanning Electron Microscope (SEM) was used in order to either access to magnifications not available in an optical microscope or to identify the secondary phases or the nature of defects. Furthermore, the backscattering mode enables distinguishing the presence of secondary phases, and the EDX analysis is crucial in order to identify the nature of such secondary phases.

Additionally, a more detailed study of the microstructure was also performed in some welded samples of several misorientation angles. The distribution of the Y_2BaCuO_5 (known as Y-211 or green phase) particles, the formation of cracks, the influence of the misorientation on the microstructure and the weld shape were characterized in some samples. The information obtained from this study has been crucial for a better understanding of the welding process.

5.1 Sample preparation

A proper observation of the samples using the optical microscope requires a scratch free and clean surface. For that reason, the sample surface to be observed must be carefully polished. This polishing operation has been carried out using silicon carbide abrasive disks with grit sizes of 320, 500, 800, 1000 and 1200 (grain sizes from 31μm for the 320 case to 7μm for the 1000 case). Water has been used as a refrigerant. The sample is cleaned with acetone before polishing it with the next disk, thus avoiding the contamination of the disk by particles coming from the previous one. This cleaning also minimizes the contact between YBCO and water, so formation of carbonates that would degrade the material is mitigated.

The grade of polishing is then refined using textile disks with diamond powder of grain sizes of 9, 6, 3 and 1μm. In this case, water must be completely avoided and an ethanol based refrigerant liquid is used instead.

At the end, the sample is submerged in ethanol and an ultrasound cleaning is applied in order to wipe out undesired particles, produced during this polishing process.

Additionally, the details of the surface being observed can be enhanced by chemically etching that surface. This is carried out by submerging the sample with 10% diluted acetic acid for 30-60 seconds; afterwards, the sample is cleaned with ethanol.
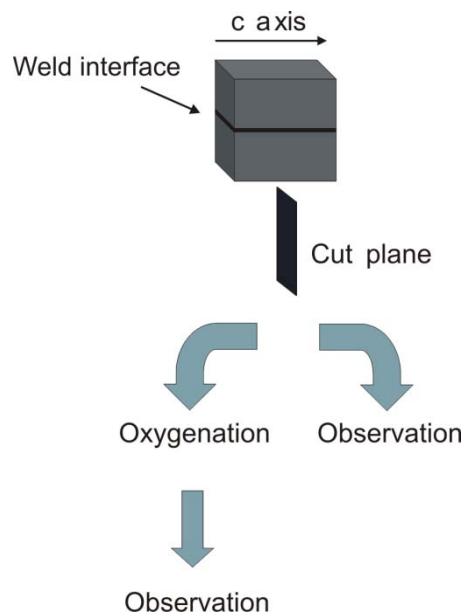
FIGURE 5.1 SAMPLE CUTTING SCHEMA FOR THE MICROSTRUCTURAL STUDY.

For the current study, samples with both tetragonal and orthorhombic state have been considered. Each sample being included in this work is cut into two parts as schematized in Figure 5.1. One part is then oxygenated and observed. This oxygenated part is also used for the magnetic characterization that will be discussed later in Chapter 5.

5.2 Basic characterization

A basic characterization is systematically carried out for all welded samples in order to ensure a proper formation of the weld. At the same time, the exact misorientation introduced is determined by measuring the misorientation angle between the twin planes at both sides of the weld.

In this basic characterization, four possible formation anomalies can be easily detected: Non-molten silver, secondary phases at the weld interface, voids due to a defective contact between the single domains and poly-crystallinity.

5.2.1 Visual weld quality evaluation

In the case of a non-optimized thermal process, some of the above anomalies can be present in the microstructure. If the maximum temperature has been too low to achieve a complete melting of the silver foil, at the end of the thermal process, the weld zone is still occupied by a large amount of unreacted silver (see Figure 5.2).
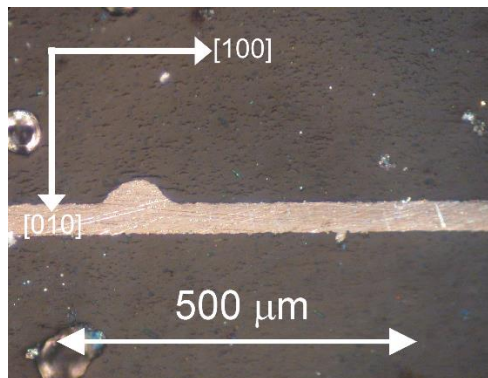
FIGURE 5.2 DETAIL OF A WELDED SAMPLE WHOSE TEMPERATURE WAS TOO LOW TO ALLOW THE FULL MELTING AND POSTERIOR REACTION OF THE SILVER, THUS LEADING TO A SIMPLE MECHANICAL UNION.
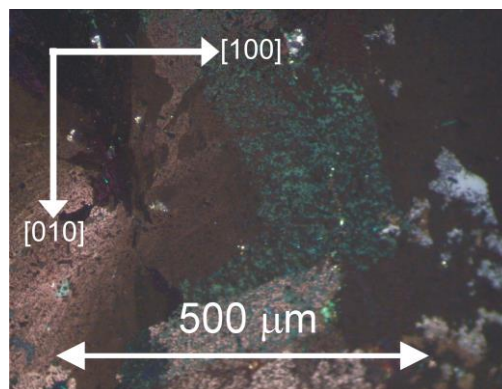
FIGURE 5.3 ZONE OF THE SAMPLE WHERE THE TEMPERATURE HAS BEEN TOO HIGH AND LEADED TO AN EXCESSIVE MELTING OF THE MATERIAL. SINCE THE TEMPERATURE WINDOW IS NOT OPTIMIZED FOR THE Y-123 PHASE, THE RE-SOLIDIFICATION LEADED TO THE FORMATION OF A POLYCRYSTALLINE ZONE.

In contrast, if the temperature is higher than the temperature where the Y123 → Y211 + L pseudo-peritectic reaction occurs, a wider range of material is molten. In the first stage of the thermal process, a fast cooling is carried out down to 980°C, so the molten zone becomes polycrystalline. This is the case observed, for example, in Figure 5.3. The image is taken using a light polarizer, so that the brightness of the image is different depending on the crystallographic orientation of the sample. This mosaic like aspect of the image reveals that the explored zone is composed by different crystals.

a)   b)

c)
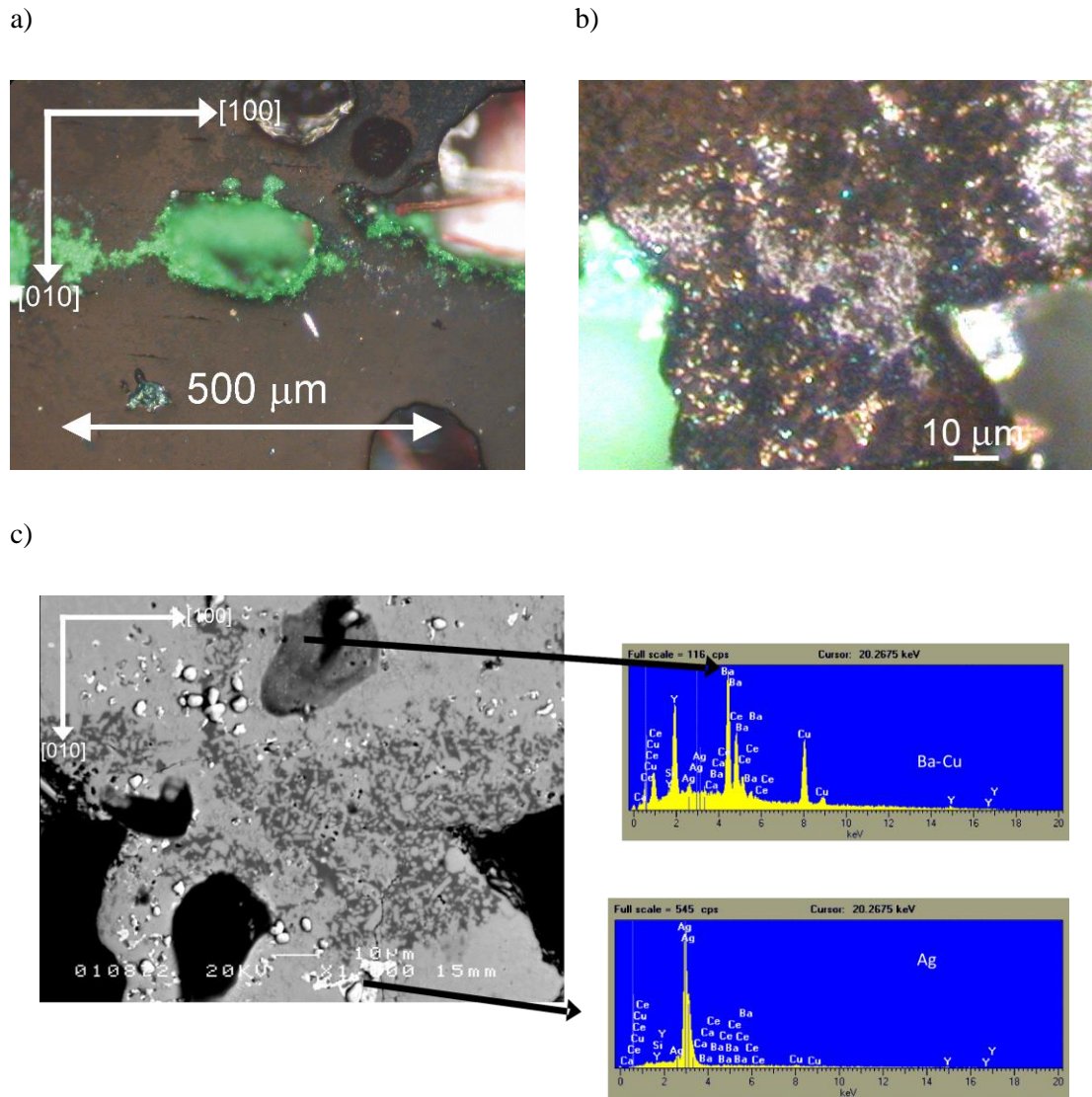
FIGURE 5.4 (A) DETAIL OF A DEFICIENTLY REACTED WELD ZONE, WHERE THE L' LIQUID WAS DISPLACED AND A HUGE AMOUNT OF Y-211 PHASE REMAINED UNREACTED. (B) DETAIL OF ANOTHER ZONE OF THE SAMPLE, WHERE A CONSIDERABLE AMOUNT OF SILVER INCLUSIONS CAN BE OBSERVED. (C) BACKSCATTERED SEM IMAGE OF THE SAME ZONE, WHERE SEVERAL PHASES CAN BE DISTINGUISHED.

At the same time, with this visual evaluation, unreacted phases that would indicate a not optimum distribution of the L' liquid during the weld formation can be detected. Those phases can be present either because the liquid has been excessively dragged out or because it simply got distributed irregularly along the molten zone. This anomaly was frequently present at samples that were welded without the MgO plates.

Other secondary phases, though, cannot be easily detected in optical microscope pictures and the use of SEM backscattered images can complement the information. This is the case presented in Figure 5.4b and Figure 5.4c, where a rich collection of secondary phases can be found. In the optical microscope image, only Y-211 and silver inclusions are observed, whereas if the same sample zone is observed in the backscattered SEM image, other secondary phases are detected. In this SEM image, three gray tones can be observed. The darkest one, if an EDX analysis is carried out, reveals that there is an increased amount of Ba and Cu, compared to the normal levels present for the Y-123 phase. This fact indicates that a considerable amount of liquid did not react with the Y-211 phase. The EDX analysis on the lightest parts of the SEM image confirms that the bright spots observed in the optical microscope picture are silver inclusions inside the Y-123 matrix (medium dark zones in SEM image).

Obviously, the ideal case for a properly formed weld is that the microstructure exhibits no difference between the normal Y-123 matrix and the welded zone (Y-123ss phase). In Figure 5.5, such a case is shown, indicating that the thermal treatment and L' distribution was correct.
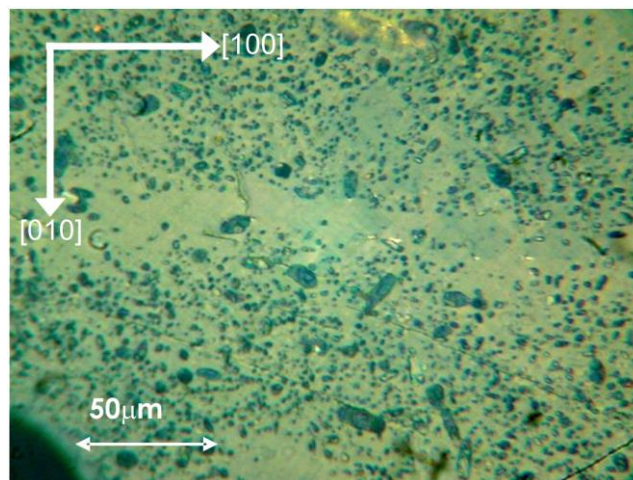
FIGURE 5.5 DETAIL OF THE WELD ZONE FOR A PROPERLY FORMED WELD. THE WELD IS SITUATED AT THE Y-211 QUASI-FREE ZONE. THE IMPLICATIONS OF THIS ZONE WILL BE DISCUSSED LATER IN THIS CHAPTER.

This basic observation of the microstructure is enough for determining whether a welded sample is eligible for the study of the influence of the misorientation angle between the welded tiles that will be discussed later in this chapter. For this study it is crucial to have properly welded samples under the scope of its microstructure, since any of the anomalies exposed above can severely affect the J_c^{GB} value and lead to wrong conclusions in that study.

5.2.2 Exact misorientation evaluation

The cutting method explained above, in Chapter 4, used for introducing the desired misorientation for the weld can lead to a real misorientation that can be slightly different to the one initially pretended. For that reason, a more exact method for determining this misorientation has been used.

The ab plane for oxygenated samples exhibits a presence of two sets of twin planes, with a relative orientation of 90 degrees respect to each other. The orientation of those two sets is directly related to the orientation of the [100] and [010] axes of the crystal; in consequence, measuring the relative misorientation between the sets at each side of the weld means to measure the relative crystallographic misorientation between to two welded monodomains.

In Figure 5.6, it can be observed such a relative misorientation of the twin planes at each side of the weld. In this case, the determined angle is of 10 degrees. Although the pretended angle was of 10 degrees, other cases may exhibit a real angle different from that pretended. At the end, thanks to this error, a quasi-continuous range of angles is present in the study of those misoriented welds.
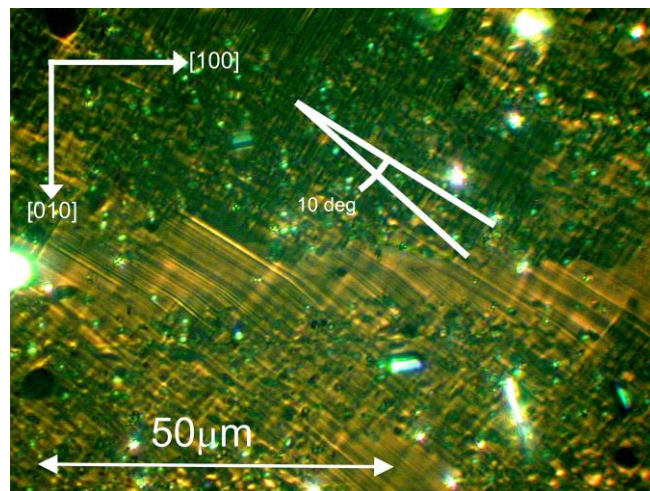
FIGURE 5.6 EXAMPLE OF A MISORIENTED WELD WHERE THE TWIN PLANES CAN BE USED TO DETERMINE THE REAL MISORIENTATION BETWEEN THE JOINED PARTS.

This basic study of the microstructure has its aim only to satisfy the first of the two main objectives of this thesis work: The study of the influence of a crystallographic misorientation on the superconducting properties of the weld. In order to satisfy the second objective: To gain a deeper understanding on the phenomena involved in the formation of the weld and, at the same time, reveal the limits of the welding methodology, a more thorough study of the microstructure has been carried out. The remaining sections of this chapter will expose the most interesting characteristics of the microstructure of the welded samples.

5.3 Y-211 particle distribution

The Y-211 phase has a crucial role in the melting and resolidification process. It is known that Y-123 phase incongruently melts following the pseudo-peritectic reaction:

$YBa_2Cu_3O_{7-\delta} \rightarrow Y_2BaCuO_5 + L' (BaO+CuO)$
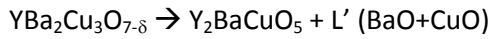
By studying how its distribution in the Y-123 matrix is modified at the welding interface will provide very useful information about the nature of the liquid present, if any, during the thermal process.

The Y-211 particle distribution was observed in both ab and ac planes (see Figure 5.7). It has to be remarked that near the weld position, the distribution of those particles is clearly modified, exhibiting an almost Y-211 free zone, in fact, only green phase particles of large size still remain. This zone, denoted as Weld Path, is clearly delimited and contains the weld interface.

a)   b)
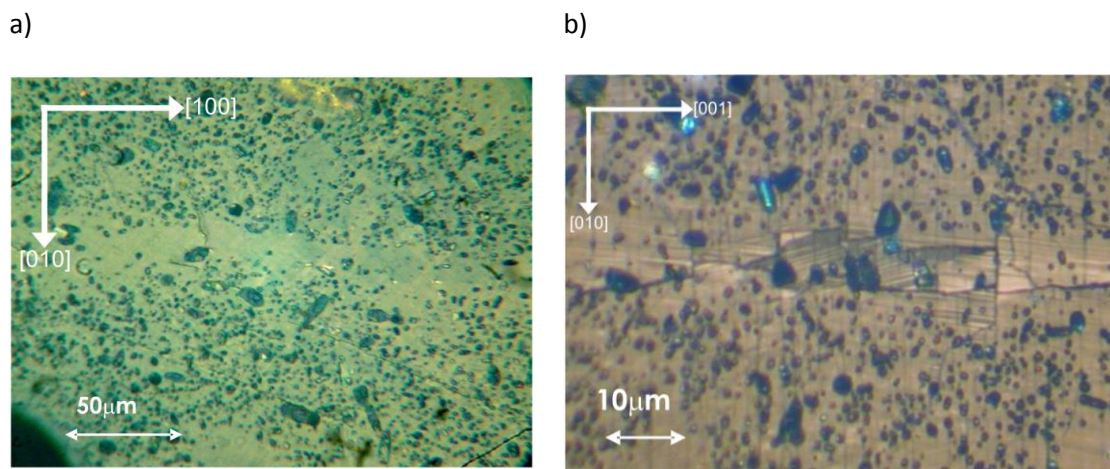
FIGURE 5.7 DETAIL OF A (001) PLANE (A) AND (100) PLANE (B) WHERE THE WELD PATH CAN BE CLEARLY DISTINGUISHED.

The absence of Y-211 particles would indicate that, during the thermal treatment, the Y content would have been depressed, remaining only a liquid with a higher quantity of Ba and Cu. So, during recrystallization, the Y-123 phase would have been restored by dissolving the Y-211 particles.

A model is later proposed in section 5.7, where it is intended to explain the origin of this Y deficiency.

5.4 Crack formation

During the basic characterization, evidences of weld cracking were found. This cracking was detected in the pictures used for measuring the misorientation between the twin planes at both sides of the interface. The basic characterization for samples in tetragonal state seldom ever presented cracking.

This cracking phenomenon must be studied in more detail, since cracking is an indication of mechanical weakness that could imply a drawback for possible technological applications of the welding technique where large magnetic fields are used, due to the high forces that are generated (52, 53).

In particular, the pieces belonging to both tetragonal parts of the samples were compared to their corresponding oxygenated counterpart. In Figure 5.8, it has been represented a (100) plane for both parts of a sample as an illustrative example. The picture on the left side of the figure shows the tetragonal part, where no evidence of cracking is observed, whereas the picture on the right side, which corresponds to the orthorhombic part, cracking is clearly evident. In that picture, apart from the normal cracking present in an 'ac' plane, cracking along the interface direction has been detected.

a)   b)
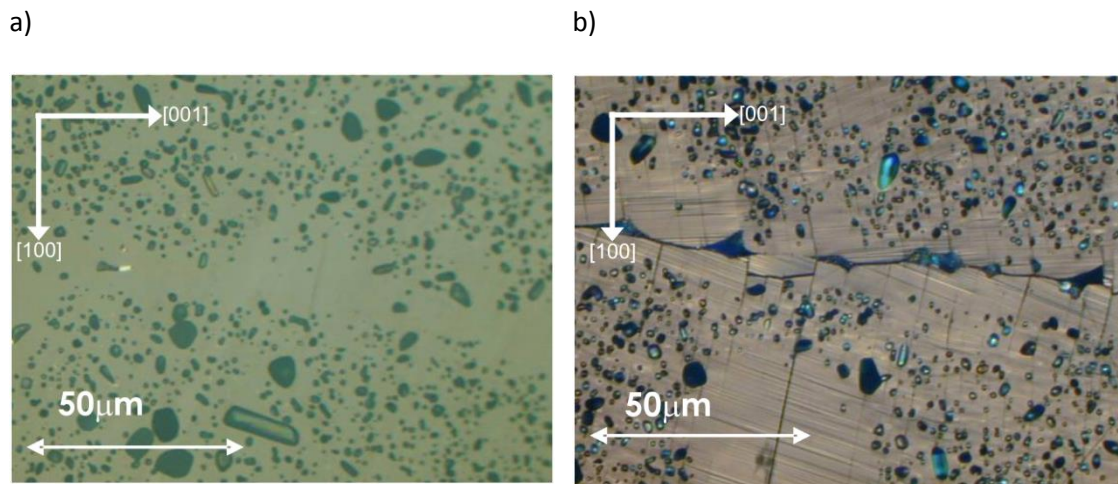
FIGURE 5.8 COMPARISON BETWEEN AN (100) PLANE CORRESPONDING TO THE PART IN TETRAGONAL STATE (A) AND ORTHORHOMBIC STATE (B)

5.4.1 Crack morphology and situation

The crack morphology and situation has been characterized. In Figure 5.9a, it has been presented an 'ac' plane, with the weld situated quasi-horizontally. It can be observed that the weld crack is situated inside the weld path zone and its continuity is interrupted by the 'ab' cracks, situated perpendicularly to it. If we observe carefully the position of the interface in relation with the crack, we can see that the weld crack is not necessarily situated at the interface.

54
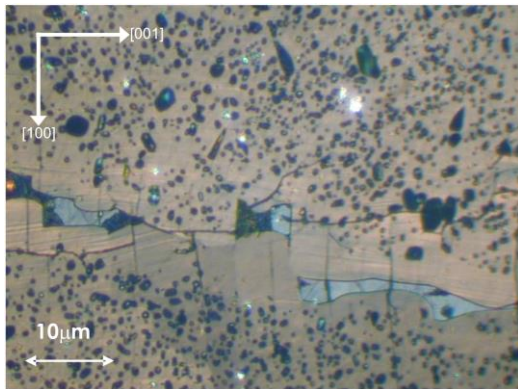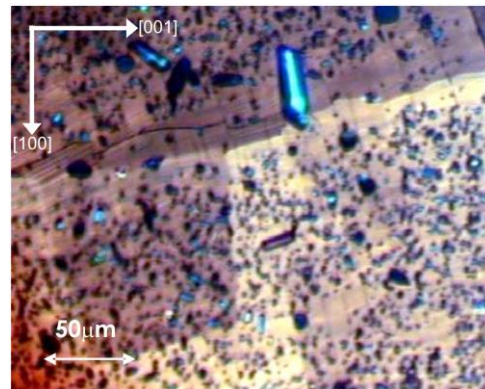
FIGURE 5.9 WELD CRACKING DETAIL. (A) CRACK CONTINUITY INTERRUPTED BY AB CRACKS. (B) SITUATION OF THE WELD INTERFACE IN RELATION WITH THE CRACK POSITION; CRACK IS PARALLEL TO THE INTERFACE BUT NOT SITUATED ON IT.

5.4.2 Influence of the misorientation angle on crack formation

In the former section, it was stated that the stresses were relaxed inside the weld path zone by the formation of cracks. It is important to study the influence of the misorientation angle on the formation of the crack. In Figure 5.10, it has been presented four different (001) planes corresponding to four different misorientation angles. By observing the twin planes, the interface position can easily be located.

The case presented in Figure 5.10a, corresponds to a welded sample with a misorientation of 7 degree. Several crack free interface zones can be located. In the picture, they have been signaled by empty circles. The crack presents a non-continuous morphology and it is not situated at the interface. The situation is not different for the 10 degree case (Figure 5.10b). Several crack free interface zones can be easily located. It should be noted in that figure, that the zones where the orientation changes do not follow a straight line. This fact would indicate a non-straight morphology of the interface; this morphology will be discussed later in section 5.5. As the angle is further increased, the probability of forming a crack at the interface position is higher. In Figure 5.10c a weld with a misorientation of 15 degree is presented. The crack in that sample is situated at the interface, but there are still zones with a crack-free interface (signaled with circles). Finally, in Figure 5.10d, the extreme case of a 31 degree weld is presented. In that case, the interface is completely cracked.

In the framework of possible industrial applications, not all the misorientations are convenient, since this cracking phenomena implies a mechanical weakness and, furthermore, a reduction of the current density across the weld to zero. Specifically, welds with misorientation lower than 15 degrees can safely be formed without introducing high mechanical stress.
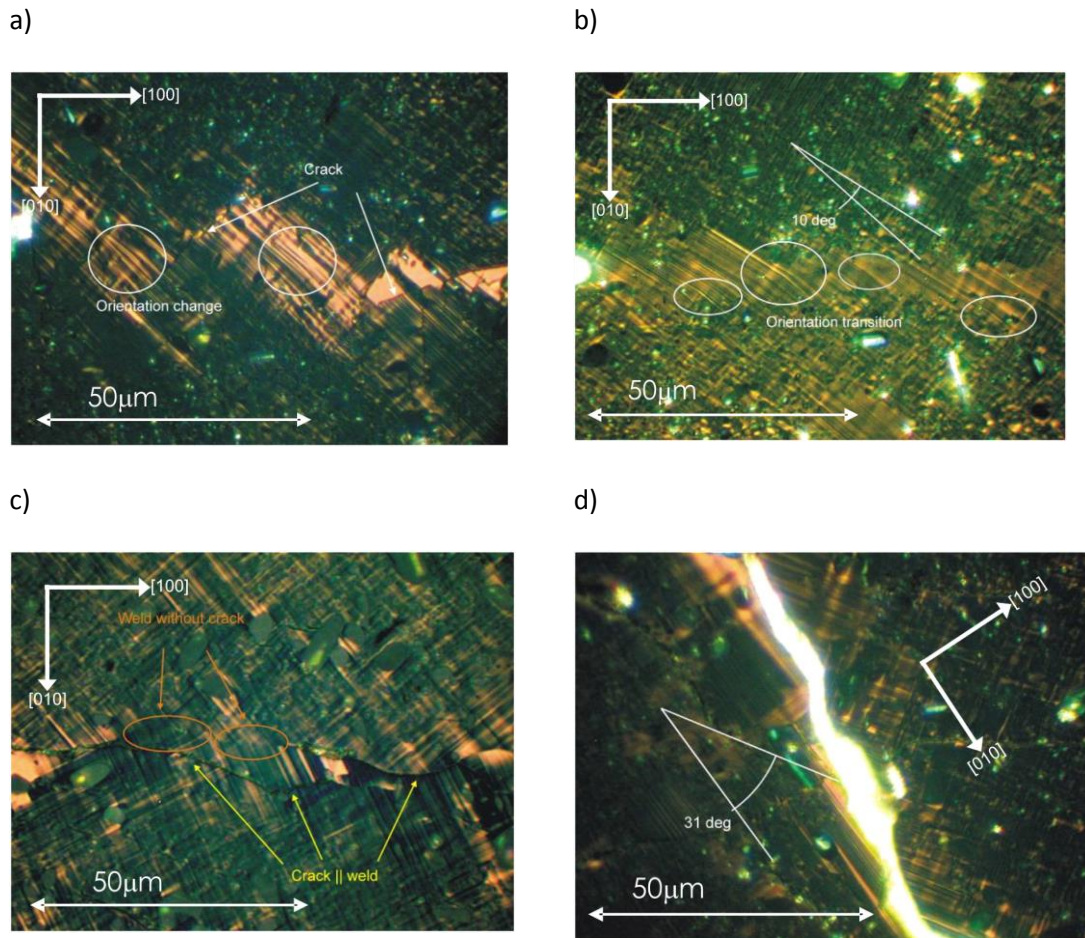
FIGURE 5.10 CRACK FORMATION FOR FOUR DIFFERENT DISORIENTED WELDS: (A) 7 DEGREE, (B) 10 DEGREE, (C) 15 DEGREE AND (D) 31 DEGREE.

5.5   Weld morphology

In the previous section, it was provided the evidence for the existence of non-straight shapes of the welds interfaces. By observing carefully the interface in polarized light this evidence is confirmed. The image presented in Figure 5.11 is a clear example of this interface morphology. The change in tonality indicates the interface position. It can be observed that this interface exhibits an irregular morphology, modulated by the presence of Y-211 phase particles. In an absolutely Y-211 free scenario, during the recrystallization of the material, the growth front would advance planarly until it finds the growth front belonging to the opposite piece. In that case, the interface would exhibit a straight structure.

The situation is indeed different, when a certain amount of Y-211 particles is present. In that case, the bigger Y-211 particles would be trapped by the growth front and, at the same time, would slow down the growth rate in their surroundings, thus deforming the growth front, ending into that wave-like shape.
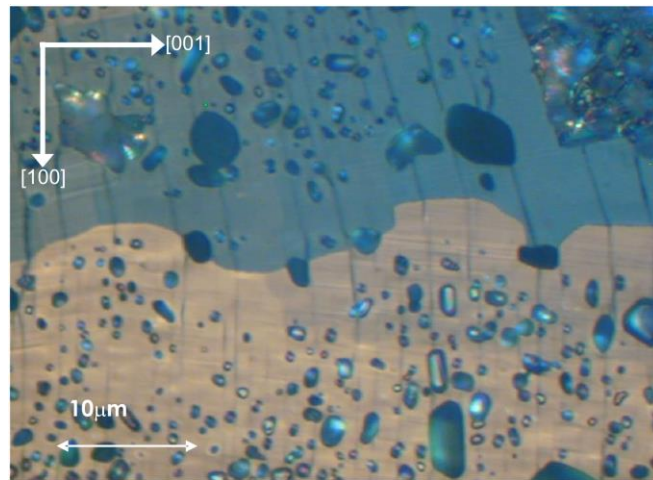
FIGURE 5.11 WELD INTERFACE DETAIL. THE Y-211 PARTICLES ACT AS PINNING CENTERS, AND PREVENT THE GROWTH FRONT FROM ADVANCING NORMALLY, CREATING A WAVE-LIKE MORPHOLOGY.

5.6 Intrinsic misorientations

In the present work, only [001]-tilt misorientations were pretended. However, during the study of the microstructure, a deviation of the ab cracks was observed in several samples (see Figure 5.12a). This crack orientation refracting phenomenon is an indication of a non-desired [100]-tilt misorientation. A more accurate observation of the (100) plane reveals that the sample presents some mosaicity (Figure 5.12b). This mosaicity is present even in zones far from the weld path, indicating that this granular characteristic of the sample is intrinsic to the material and has not been introduced during the thermal treatment used for welding the tiles.
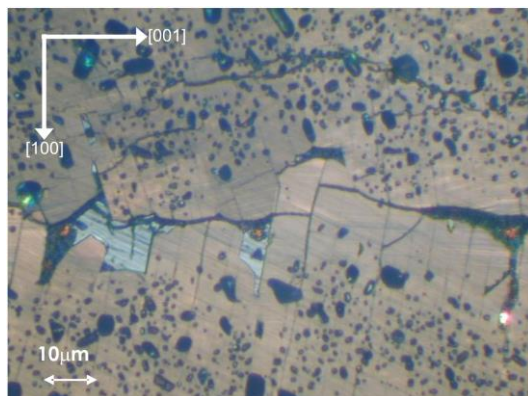
a)   b)
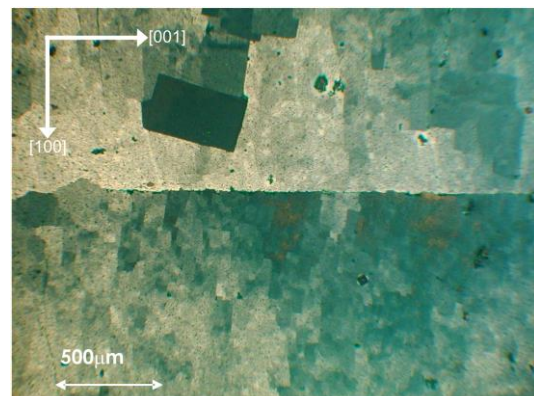
FIGURE 5.12 (A) DETAIL OF A (100) PLANE WHERE THE CRACKS PARALLEL TO [100] DIRECTION REVEAL AN INTRINSIC [100]-TILT MISORIENTATION OF A CONSIDERABLE ANGLE. IF THE SAME PLANE IS OBSERVED WITH LESS MAGNIFICATION, POLARIZED LIGHT REVEALS A MASSIVE PRESENCE OF SUB GRAINS OVERALL THE SAMPLE (B).

The presence of this mosaicity implies that it is almost impossible to have a pure [001]-tilt misorientation, as pretended in principle. It is more accurate to consider a [001]-tilt, mixed with arbitrary [100]-tilt and [001]-twist misorientations.

5.7 WORK 4: Influence of crystal plane on the welding quality of YBCO bulk superconductor

The Y-211 free zone present at the weld zone is a puzzling observation and an explanation based on the YBCO-Ag phase diagram is seeked. At the same time, since the plane used so far as the welding plane ('ac' plane) is known to be a second cleavage plane for the Y-123 system, the chance of crack formation at the weld position is considerable. In consequence, it would be interesting to investigate the consequences of changing the weld plane to a plane that it is not known to be a cleavage plane. One candidate would be the (110) plane.

All the observations carried out have been done with oxygenated samples.

The use of a different welding plane implies some changes on the local microstructure of the weld that are summarized below:

(100) welds: Weld plane is easily located by observing the Y-211 free already introduced above. In the case when the Ba-Cu rich liquid remain unreacted, it forms a film along the weld position. Cracks parallel to (100) plane are often formed and their continuity is interrupted by the presence of the cracks parallel to the (001) plane.

(110) welds: Although the Y-211 free zone is also present if the chosen weld plane is (110), some differences on the Ba-Cu rich liquid and crack formation can be observed. For the case of the unreacted liquid, it no longer forms a film-like shaped morphology. It forms a granular structure instead. Cracks are not present with this weld orientation.

The change of the weld plane would be useful to mitigate the formation of potential defects that could lead to a partially successful weld or, in the case of a successful weld, to mitigate the appearance of cracks during the oxygenation process.

The origin of the Y-211 free zone could be explained by a lower content of the Y during the recrystallization process. By inspecting the YBCO-Ag phase diagram (see Figure 5.13), at 940°C at the Ag/Y-123 interface the L'' appears, even though the Ag film is still solid.

Part of the Ag would diffuse into the Y-123, thus, lowering its melting point down to 980°C. At that temperature, the Ba-Cu rich liquid L' develops. Observations on the sub-grain structure (see Figure 5.12b) reveal that no modification on that structure occurs. This fact indicates that the molten zone has really a small thickness, less than the observable dimensions with an optical microscope. The assumption that all the molten liquid mass, including Ag, L'' and L' remains at the weld place contradicts this observation. So, it could be postulated that:

- Only a small amount of L' is produced
- L'' and molten Ag must be dragged out from the weld position. This fact could explain the nature of the liquid observed in the movies produced by the in-situ observation setup formerly discussed in section 4.2

Additionally, the postulation that the L'' contains a higher proportion of Y/Ba-Cu than that present in the Y-123 phase could explain the absence of the smallest Y-211 observed in the

weld path. The deficiency of Y at the weld path could be compensated by dissolving the Y-211 phase.
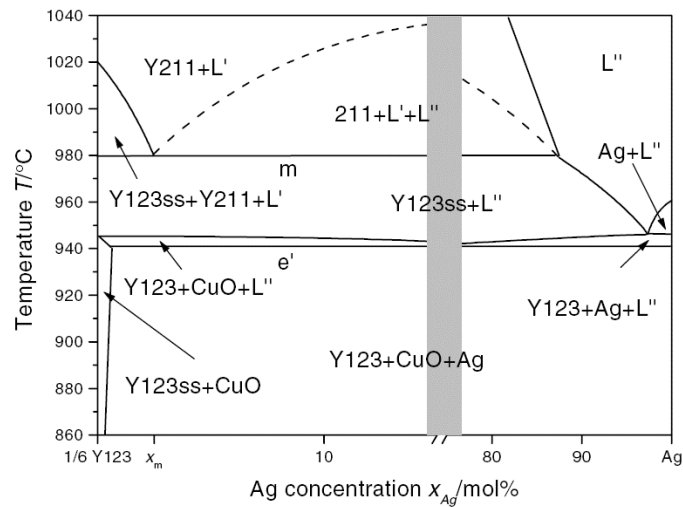
FIGURE 5.13 YBCO-AG SYSTEM PHASE DIAGRAM

5.8 Summary

In this chapter, a study on the microstructure of the samples was carried out. A basic observation of the welded samples was done in order to ensure a proper formation of the weld, and discard those cases whose weld quality would be decreased due to the presence of secondary phases, voids and cracks. This prior selection is important for the magnetic and electric properties investigation that will be reported in next chapter, in order to avoid considering factors that could obscure the results.

At the same time, in this basic observation, the real misorientation angle was determined. Although in principle, the study included only pretended 5, 10 and 15 degree [001]-tilt misorientations, the method used for shaping the pieces to join introduced a slight deviation from the pretended angle, ending up to a quasi-continuous range of angles.

Later, a carefully chosen set of samples was included in a more thorough study of the microstructure at the weld zone proximities revealing surprising results, such as a depression of the presence of Y-211 particles, thus defining a well delimited zone around the recrystallized zone, called weld zone.

For samples in orthorhombic form, a new set of cracks were discovered at this weld path zone, indicating a potential weakness of the mechanical properties of the welds. The influence of the misorientation angle was, then, studied, revealing that there is an upper limit in the misorientation angle where the weld is no longer strong enough in the framework of the mechanical properties.

Finally, the choice of another weld plane that it does not coincide with a cleavage plane for the Y-123 system would help to reduce potentially detrimental issues that can develop during both the weld formation process and the oxygenation process.

WORK 4:

"Influence of crystal plane on the welding quality of YBCO bulk superconductor"

M. Sefciková, P. Diko, B. Bozzo, X. Granados, X. Obradors

Chapter 6.   Magnetic characterization

6.1 WORK 5: In-field magnetic Hall Probe microscopy studies on YBa$_2$Cu$_3$O$_7$ based superconductors

The nature of the samples used in this work requires a suitable magnetic characterization tool. Magnetization can be measured using very and different techniques. In this particular case, macroscopic values of magnetization do not provide enough information to be correlated to other characterizations made on welded samples.

For that reason, DC extraction magnetometers or VSM magnetometers cannot be used and techniques that evaluate the local magnetization will be used instead.

Several options can be potentially useful for this purpose. Magneto-optic techniques can provide high resolution magnetization maps. However, the ferromagnetic garnet used in that technique is easily saturated (typically for induction values of 0.2T). YBCO samples typically exhibit magnetization values that overcome this induction top value.

The system used for the measurement of the magnetic properties of the samples is based on Hall Effect. The system used in the present work was built in ICMAB and consists of an AsGa Hall Probe with an active area of 0.1x0.1mm^2. The probe has been situated at the end of an arm, which it is moved by two step motors. This allows scanning a surface that can be as extensive as 50x50mm^2 with a spatial resolution that can be as fine as 32μm, although the system is normally operated with a spatial resolution of 160μm. The typical gap between the probe and the sample surface is 80-100μm. The system noise has been determined as 0.4μT (measured in the interval of 2mHz to 10mHz). In Figure 6.1, a schema of the device has been represented. The setup is inserted into a cryostat filled with boiling nitrogen. All the setup is situated in the gap of an electromagnet. This enables the application of external magnetic fields from approximately -800 to 800kA/m ($\mu_0 H$=-1T to $\mu_0 H$=1T). The whole system is

controlled by a computer equipped with the appropriate software that controls the step motors and records the signal from the Hall Probe.

From the data generated, consisting of a matrix of induction magnitude B(x,y), the local magnetization can easily be obtained by subtracting the applied field H. This is an immediate operation since the applied field is uniform at the working space. Macroscopic magnetization can still be obtained by integrating the M(x,y) map over the scanned area.
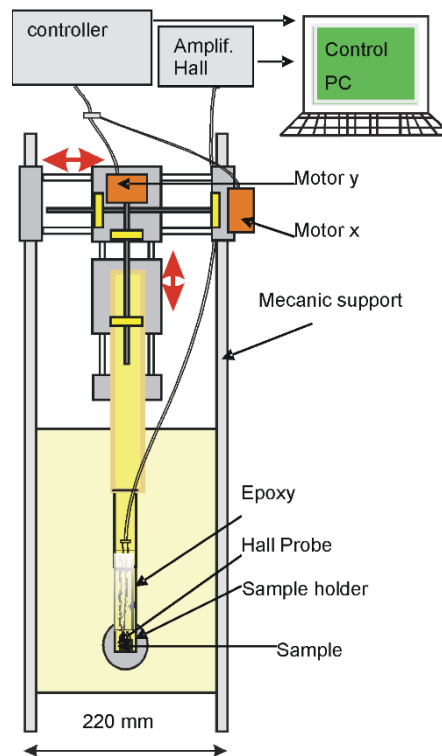
FIGURE 6.1 A SCHEMA OF THE HALL PROBE DEVICE, WHERE THE SAMPLE SPACE, HALL PROBE AND THE TWO STEPPING MOTORS ARE SHOWN

At the early stages of the development of the Hall Probe raster, the macroscopic magnetization magnitude obtained from the integration of the M(x,y) maps was compared to that obtained from an extraction magnetometer such as a Quantum Design MPMS magnetometer. That comparison provided the conversion factor between the voltage generated at the Hall Probe and the correct value of the B magnitude.

Once calibrated, this setup has been used for several applications such as:

- Superconducting melt-textured rings
- Superconducting foams
- YBCO superconductors with patterned holes
- Epitaxial YBCO thin films and coated conductors
- Melt-textured YBCO/Ag/YBCO artificial welds

For all the above listed cases, it is interesting to obtain the critical current distribution from the M(x,y) maps. This was carried out by using specially developed software that solves the inverse of the Biot-Savart law (*54*).

In particular, those critical current distribution maps were used to characterize the quality of the welded samples and that information was used as a feedback for the optimization process of the welding methodology. The system could successfully distinguish between a successfully formed weld from a weld with depleted superconducting performance.

Evaluating the weld quality from those maps was not trivial and a thorough study on the nature of those current density distributions was needed and will later be discussed in sections 6.2 and 6.3.

6.2 WORK 6: Simulation of dc magnetic effects due to geometrically defined grain boundaries in type-II superconductors

In order to study the influence of non-superconducting obstacles embedded into a superconducting sample on the shape of the trapped field a software package called "Trazacorrientes" has been developed.

That software is able to simulate how the current density is distributed in theoretical superconducting space. The simulation is carried out by tracing the current loops that are compatible with the geometry of the sample and the non-superconducting zones in it.

6.2.1 General overview

The sample is modelled as a virgin two dimensional space, surrounded by limits that do not allow the currents flow through them. Additionally, several non-superconducting obstacles that block the flow of the currents can also be added. So, the simulation space is built from an *m* by *n* matrix, initially filled by "0" for superconducting zones and "-1" for non-superconducting zones.

In a superconducting sample, if we apply a small external field, the sample response will be an appearance of a shielding current located at its most external layer. By increasing that external magnetic field, more current loops are created until the whole space is filled by currents.

The current pattern will consist of closed current loops that must follow the criteria that its inner area must be as large as possible. For that reason, the first loop will follow the shape of the external area filled by -1s, the second loop fill follow the shape of the first loop and so on. At the end, the result will be a simulation of how the current pattern would be after slowly increasing the external magnetic field for a sample that has been cooled with a null external field.

6.2.2 Program elements

6.2.2.1 Cursor

The drawing is started in a certain position and advances accordingly to the conditions of the two dimensional space. The position corresponding to the last filled matrix element has been called "cursor".

6.2.2.2 The movements

The current loops are drawn following a step by step schema. Only four movements are allowed: upwards, downwards, leftwards and rightwards. Each movement consists of a vector that modifies the coordinates of the cursor, thus generating a new cursor position. Every time the cursor position has been modified by the movement vectors, the corresponding cell is marked by the value of the loop level: 1 for the first level, 2 for the second, and so on. The current movement is controlled by a numeric variable that takes 1 for rightwards, 2 for upwards, 3 for leftwards and 4 for downwards.

6.2.2.3 Exploration matrix

In order to control and decide what it is the next action the program will perform, a 3x3 matrix is used. That matrix takes the values of the two dimensional space around the cursor and allows checking whether there are obstacles in the next cell to draw or not. According to the -1 distribution values found in the exploration matrix, the movement direction will be changed or not.

6.2.2.4 Movement selector

It consists of a set of matrices of the same dimensions as the exploration matrix. Each of them is filled with zeros except for a single 1 in a different position for each available movement (see Figure 6.1).

a)

0	0	0
0	?	1
0	0	0

b)

0	1	0
0	?	0
0	0	0

c)

0	0	0
1	?	0
0	0	0

d)

0	0	0
0	?	0
0	1	0
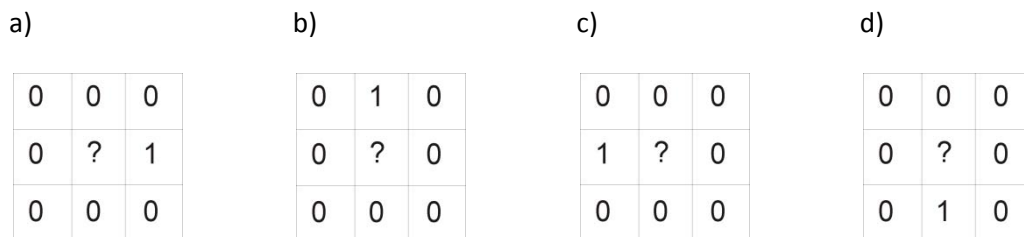
FIGURE 6.1 MOVEMENT SELECTOR MATRICES.

6.2.3 Drawing current loops

The drawing is started at the bottom-left corner of the space. The program first looks for the first position near to that coordinate for a "0" filled cell. The starting movement is rightwards. In order to achieve the condition of maximal inner area, the exploration matrix is multiplied element by element with each movement selector, starting with the matrix corresponding to the current movement index-1 and finishing with current movement index+2 (for example, if current movement is 1, the order is 4, 1, 2 and 3). The first movement selector that causes this multiplication to become null corresponds to the next movement that the program will perform. This algorithm ensures that the current loops will meet the condition of maximum inner area.

The program will continue exploring, selecting and advancing to next position until the loop has been closed. The program will, then, check whether there are more loops to draw in the current level and start a new loop if so. Once there are no more possible loops to draw in the current level, the program advances to the next level and starts the algorithm again. The

simulation finishes once all the superconducting space has been filled. The program diagram flow has been presented in Figure 6.2.
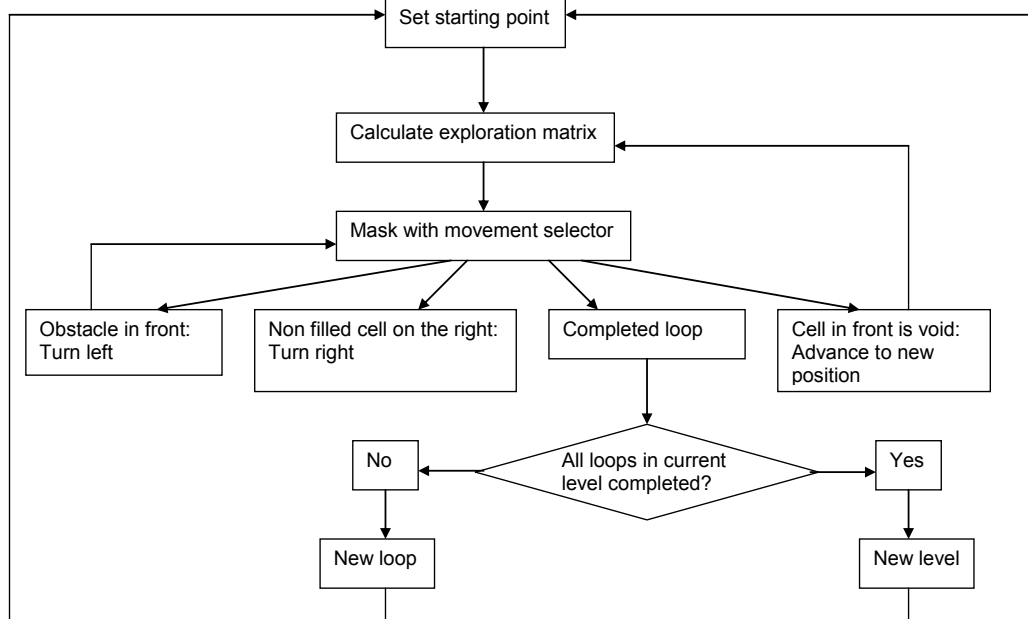
FIGURE 6.2 CURRENT TRACER PROGRAM FLUX DIAGRAM

6.2.4   Application to the weld problem

The software piece was proven to be useful for simulating a wide range of situations due to the fact that it does not need to assume any particular starting conditions when the loop drawing starts. However, its main purpose was to simulate the shape of the critical current distributions for the case of two single crystals with a grain boundary between them.

Grain boundaries were simulated as an alternating pattern of superconducting and non-superconducting zones. The first stages of the simulation already showed that the resulting map shapes were consistent with the observations performed using magneto-optic techniques on bi-crystals.

On a later stage, grain boundaries were modelled using a more realistic schema. Grain boundaries exhibit a meandering aspect. In the case of Trazacorrientes, this meandering shape was modelled by assembling several straight line facets with arbitrary angular misorientation from one sketch to the next. This caused the appearance of a stair shaped effect on the current distribution that became more important as the faceting shape was increased.

Artificial welds can be modeled as grain boundaries, since in general; the weld zone can behave like a grain boundary under the scope of its superconducting properties. This fact becomes especially true for the case of disoriented welds where an artificial grain boundary is necessarily formed.

In order to be able to determine a figure of merit for the weld quality, several weld qualities, modelled as grain boundaries with different alternating superconducting/non-superconducting

patterns were simulated. The knowledge acquired from those simulations was highly useful for developing a suitable analytic method for determining the intra- and inter-granular critical current density.

6.3 WORK 7: Determination of the inter- and intra-granular critical currents in superconducting YBa$_2$Cu$_3$O$_7$ welds

It is known that the current density is one of the most important magnitudes for evaluating the quality of a superconducting material, since many applications are based on the quantity of current that the material is able to carry without dissipation. The case of welded samples is not an exception. For that reason, the necessary methodology for evaluating the quality of the weld in terms of current densities has been developed.

That methodology allows determining simultaneously the J_c^{GB} and J_c^{G} current densities. It is based on the analysis of the current density distribution expected for a two-domain block; derived from the Bean critical state model (5), as described below.

6.3.1 Current distribution for a two-domain block under the scope of the critical state

The Bean Model applied to a type II superconductor assumes that the current density is constant overall the sample. Although this assumption is not fully true for a real case, the Bean Model is a valid approximation in order to understand how the current density is distributed and, specially, how to extract useful information from that distribution.

In the framework of the same model, the case of a two-domain block can be also considered. In this case, the sample exhibits two current density values: The current density that the domain interface is able to allow to cross (inter-grain current density) and the current density that the rest of the material is able to support (intra-grain current density). The expected current density pattern for a two-domain block is the one presented in Figure 6.3.
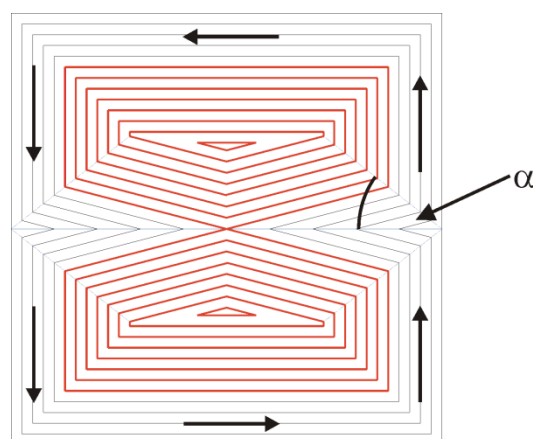
FIGURE 6.3 CURRENT LINES FOR A TWO DOMAIN BLOCK AS PREDICTED BY BEAN MODEL

It can be appreciated that the current density lines bend at the grain boundary region with an angle α that it is directly related to the J_c^{GB}/J_c^{G} ratio as follows:

$$\cos 2\alpha = \frac{J_c^{GB}}{J_c^G}$$

<div align="right">**6.1**</div>

In the case which has been presented in Figure 6.3, the J_c^{GB}/J_c^G ratio is 0.25. So, from equation 6.1, it can be inferred that $\alpha=38°$. The flux penetration in the domain interface is faster than that in the rest of the material. Therefore, two kind of current loops can be distinguished: Those extending overall the sample, and those circulating only inside the grains. The formation of the two unconnected current loops is, hence, dominated by the dimensions of the two-domain block and the J_c^{GB}/J_c^G ratio.

The J vector can be decomposed in two components: The component parallel (J_x) and perpendicular (J_y) to the interface. Depending on whether those components have null values or not, several zones can be defined. As it can be observed in Figure 6.4a, there exist 6 zones where the current density vector is formed only by the J_x component (shaded in orange) or J_y component (triangular shaped and red shaded). There also exist 4 zones in the central part of the figure where the J vector consists of a mixture of J_x and J_y components (green). The intra-granular current density component (J_c^G) can easily be determined from the J_x and J_y values: The values of J_x in orange zones and the values of J_y in red zones directly correspond to the intra-granular component. The inter-granular component can be determined from either J_x or J_y values in green zones. However, the determination of J_c^{GB} from J_y can be performed directly without the need of further calculations.
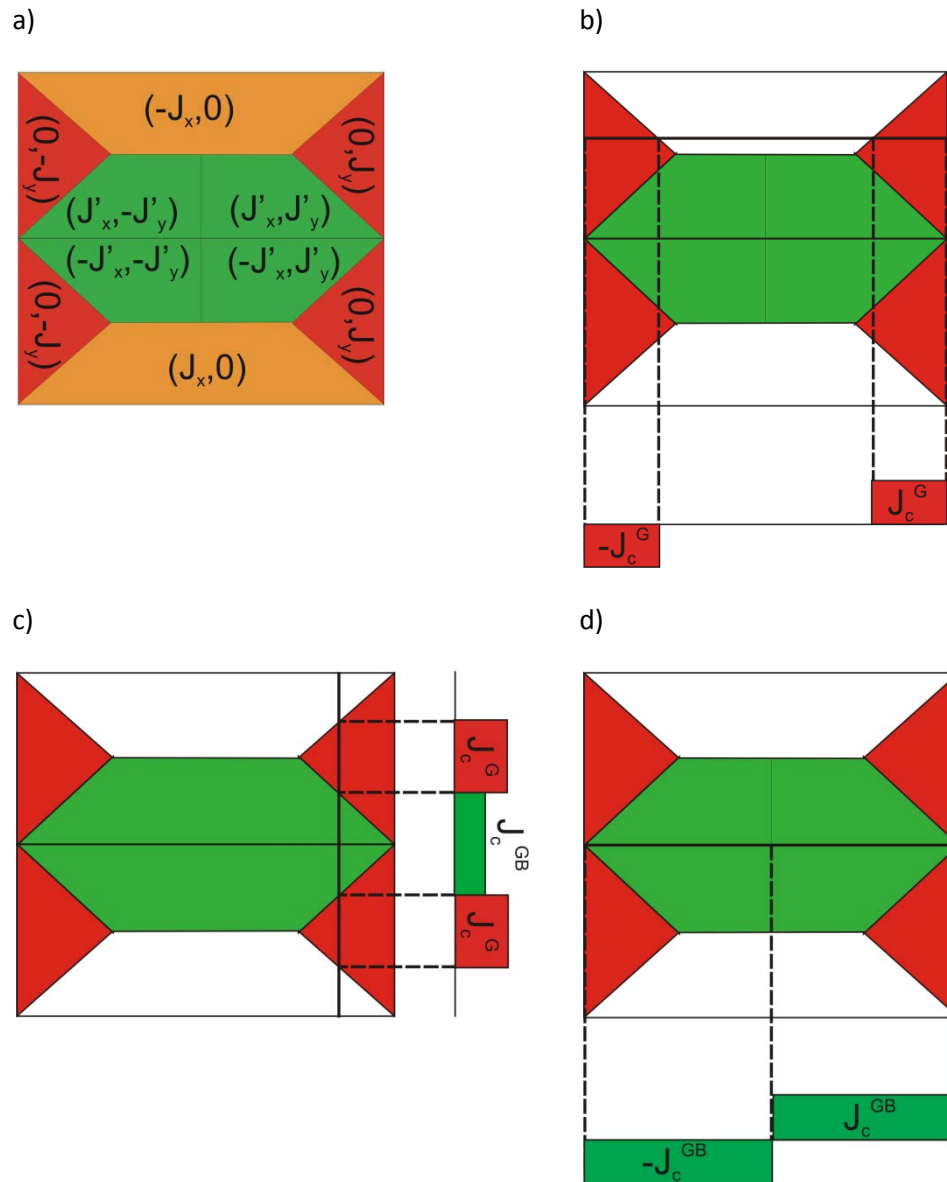
FIGURE 6.4 DECOMPOSITION OF THE *J* VECTOR INTO J_x, AND J_y (A). THE THREE PROFILES USED IN ORDER TO DETERMINE THE J_c^{GB} AND J_c^{G} VALUES ARE REPRESENTED: (B) DETERMINATION OF THE J_c^{G}, LOCALIZATION OF THE WELD POSITION (C) AND J_c^{GB} DETERMINATION (D).

Hence, for simplicity, only the J_y component will be used in order to determine the J_c^{GB} and J_c^{G} components. If we trace a profile parallel to the interface, crossing the triangular shaped zones (Figure 6.4b), the result is a profile consisting of two plateaus, one positive and one negative. Those values correspond to the J_c^{G} component.

Then, the interface position is located by profiling perpendicularly to the interface and also crossing the red zones (see Figure 6.4c). The resulting profile, now, consists of three plateaus. Two of them have the same value and correspond to J_c^{G}, whereas the third one, exhibiting a lower value, corresponds to J_c^{GB}. Finally, obviously, if we trace a third profile exactly on the interface position, it will consist of only J_c^{GB} values (Figure 6.4d).

6.3.2 Influence of the J_c^{GB}/J_c^{G} figure of merit on the trapped field shape

It is interesting to theoretically study the influence of the J_c^{GB}/J_c^{G} ratio on the shape of the trapped field map. In order to achieve this, a software package has been developed. For that purpose, the current tracer simulation program described in section 6.2 has been used.

Three welds exhibiting a 100%, 90% and 50% values of the figure of merit have been modelled. The welded sample has been simulated by using a 120 by 120 matrix filled by 0s split with an alternating queue of "-1"s and "0"s that simulates the weld. The figure of merit value can be tuned by varying the distance between "-1" valued pixels and its proportion with the "0" valued ones.

Once each current pattern has been built, the corresponding $B_z(x,y)$ is calculated by applying the Biot-Savart law:

$$B(\vec{r}) = \frac{\mu_0}{4\pi} \iiint \frac{\vec{J}(\vec{r}')\times(\vec{r}-\vec{r}')}{|\vec{r}-\vec{r}'|^3} d^3r' \qquad \textbf{6.1}$$

Approximating to a discrete case and to the 2D geometry of the problem, it becomes:

$$B_z(x,y) = \sum_{x'}\sum_{y'} \frac{J_x \cdot (y-y') - J_y \cdot (x-x')}{r^3}$$
$$r = \sqrt{(x-x')^2 + (y-y')^2 + h^2} \qquad \textbf{6.2}$$

The variable h is the gap distance in z direction where the magnetic field has been calculated. In Figure 6.5, it has been represented the three calculated magnetic field maps. For the 100% case, the shape of the field consists of, as expected, a single peak. The situation is different for the cases of the figure of merit with a 90% and a 50% in value. In both cases, the figure exhibits two peaks with a valley in between, indicating a depression of the superconducting properties. In the 90% case, although the values of magnetic field at the weld position remain comparable to those in the rest of the material, the shape of the map has been noticeably changed. This fact probes that the shape of the field is very sensitive to the presence of defects that slightly depress the superconducting properties. It has, then, to be taken into account that the presence of a two peaked map does not necessarily indicate a deep depression of the superconducting performance of the weld.

Since the usual situation is the opposite of the case presented above, the three calculated maps will now be used to recalculate the current density patterns. This can be achieved by using the software package "Caragol", details of which will be described later in section 6.3.4.

As expected, the $J_y(x,y)$ map for the 100% case exhibits only two triangular areas where the current density is non-null and constant for each zone (see Figure 6.5a, right panel). In contrast, in the 90% case, the superconducting performance depression is appreciated by a slight deformation of the triangular zones, even though the J values at the deformed zone still remain high (Figure 6.5b, right panel). Finally, in the computed current density map for the 50% case it can be appreciated that the two triangular zones have now been split into four

triangular zones. At the central part, there exists, now, an additional zone with a lower J value, corresponding to J_c^{GB} (Figure 6.5c, right panel).

a)
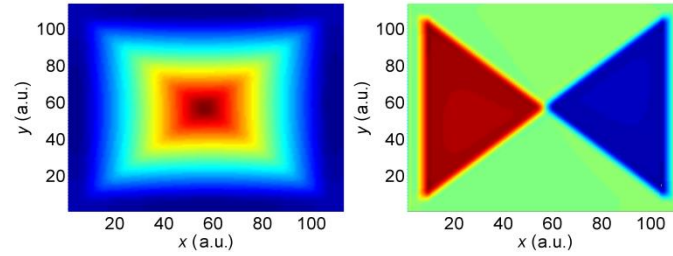
b)
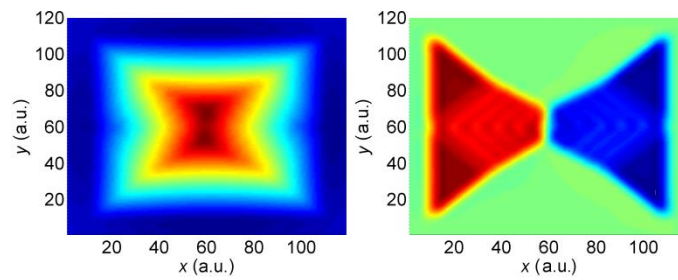
c)
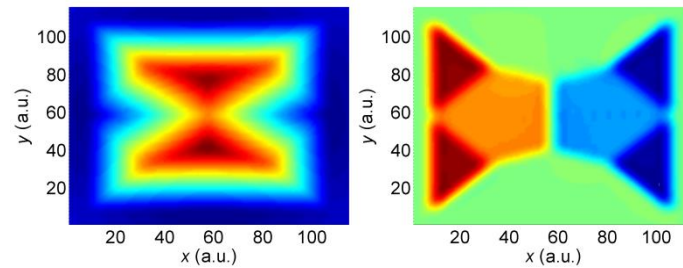
FIGURE 6.5 MODELIZATION OF THE THREE DIFFERENT WELDS WITH THEORETICAL J_c^{GB}/J_c^G RATIOS OF: (A) 100%, (B) 90% AND (C) 50%. LEFT COLUMN: SIMULATED MAGNETIZATION MAP OBTAINED FROM THE CURRENT TRACER PROGRAM. RIGHT COLUMN: CORRESPONDING $J_Y(X,Y)$ MAPS OBTAINED FROM THE "CARAGOL" SOFTWARE.

6.3.3   Magnetization measurement

6.3.3.1   Measurement protocol

The first stage of the characterization is based on the measurement of the magnetization map on a surface of the sample. This measurement is carried out, using a Hall Probe raster system whose details are described in section 6.1. In all cases in the present work, the measured surface corresponds to an ab plane with the weld plane perpendicular to it.

For the measurements made in the remanence state (field cooled measurements), a field of approximately 500kA/m (μ_0H=0.6T) is firstly applied with the device already inserted into the cryostat. The system is then cooled down with liquid nitrogen. Finally, when the temperature

of boiling nitrogen is reached, the field is removed and the measurement is started. The standard measurement is carried out with a spatial resolution of 160μm and normally takes about twenty minutes.

For some studies, it is also interesting to study the evolution of the magnetization as the external magnetic field is modified. For instance, *M*(*H*) measurements have been used in order to predict the vortex dynamics (*55*). In that type of measurements, the samples are cooled down with a null external field (the measurement is also known as zero field cooled measurement).

6.3.4 Current density calculation

In order to properly compare several samples which probably do not have exactly the same dimensions, a size independent magnitude has to be used. The data obtained from the measurement is size dependent, so a good comparison between samples becomes difficult. In contrast, the current density can be a good choice.

Current density distribution and magnetic field are related each other by the Biot-Savart law. Hence, a tool that allows obtaining the current distribution from the measured magnetic field is necessary.

In the present case, for that purpose, a software package called "Caragol" has been used. The algorithm used for calculating the current density distribution has been described in detail in (*54*). Mainly, the program uses the component which it is perpendicular to the analysed plane $B_z(x,y)$ as input and computes which current density distribution $J(x,y)$ generates the same $B_z(x,y)$ pattern. The program only makes two assumptions:

The current must be horizontal. This means that the component $J_z(x,y)$ of the current density vector must be null.

The current density pattern is planar, i.e. the $J_x(x,y)$ and $J_y(x,y)$ components only depend on *x* and *y* coordinates. So, they are constant in *z* dimension.

No further assumption is made about the geometry of the current density patterns in the *xy* plane. The first step of the algorithm consists of a re-meshing of the input data and assuming that the magnetization *M* is constant in each grid and takes *M*(*i,j*) value. In those conditions, the following equations are satisfied:

$$B_z(x, y) = \sum_{i,j} M(i, j) \frac{\mu_0}{4\pi} \int_{\Delta ijxI} \frac{3z^2 - r^2}{r^5} \, dvol$$

$$r = \left| (x_m, y_n, h) - (x, y, z) \right|$$

6.2

The integral expression of equation 6.2 depends only on the sample geometry, so it can be calculated independently. Once the integral is solved, the problem is reduced to a linear system with the matrix *M*(*i,j*) as incognita. When the *M*(*i,j*) has been determined, the *J*(*x,y*) vector can be calculated as follows:

$$\vec{J}(x, y) = \nabla \times \vec{M}(x, y) \qquad\qquad\qquad \textbf{6.3}$$

At the end, the software outputs six files consisting of: Two files for the x and y components of the current density vector, a third one for the modulus $J_v(x,y)$, another for the magnetization $M(x,y)$, a copy of the input magnetic field and, finally, the magnetic field recalculated from the $J(x,y)$ determined by the program. With that sixth file, the validity of the assumptions made by the program can be evaluated: That the magnetic field was fully perpendicular to the surface and that the current density distribution was planar. A discrepancy between the input magnetic field and the recalculated one is an indication that the calculated current density distribution does not correspond to the reality of the sample.

6.3.5   Determination of intra- and inter- granular current densities for an actual weld

The main characteristic of Bean Model is that the current distribution inside the material is a constant value, independent to the applied field, J_c, or null.

However, a real situation is more complex. YBCO pellets always exhibit some inhomogeneities in their superconducting properties, caused by many factors such as secondary phases, voids, undesired grain boundaries, etc. It is also known that J_c is indeed dependant with the magnetic field. Additionally, Bean Model relies also on the assumption that an infinitely thick sample is used, not representative for a real case. For those reasons, the assumptions made by Bean Model fail to fully predict a real situation.

A methodology for obtaining the J_c^{GB} and J_c^{G} components has been previously introduced in the current section. This methodology fully relies on the current density patterns predicted by Bean Model, so, it has to be adapted to an actual weld.

As an instructive example, we consider the case of a weld exhibiting lower superconducting performance compared to the rest of the material. In Figure 6.6, the trapped field for that weld is presented. The shape of the field map resembles to that predicted by Bean Model and presented in Figure 6.5c, as a result of the simulation explained in section 6.3.2. The difference in the real case is that the field figure presents a more rounded character than that exhibited in the simulated case.
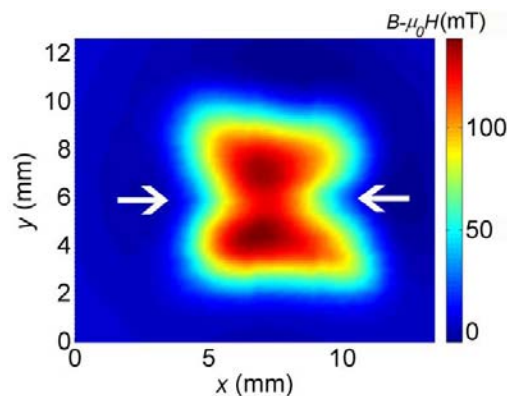
FIGURE 6.6 TRAPPED FIELD MAP FOR A SAMPLE WITH THE WELD EXHIBITING LOWER SUPERCONDUCTING PERFORMANCE

After using the Caragol software, the *J* patterns are obtained. For the reasons exposed above, only the J_y component will be used for the determination of J_c^{GB} and J_c^G.

We can proceed analogously to the methodology explained in section 6.3.1. It is expected that, since the trapped field maps have that rounded characteristics, the current density maps will no longer consist of plateaus. This fact complicates the determination of the intra- and inter-granular current densities and that methodology has to be readapted. As a workaround to the problem, two approximations have been considered and they will be explained below.

6.3.5.1   Local evaluation: Maxima method

The values are determined from the local maxima found in the J_y component maps. In Figure 6.7a typical J_y map for a real sample has been presented. The map still exhibits four triangular-like zones (labelled as "a", "b", "c" and "d").

Ideally, the values at the maxima should be the same. However, due to the intrinsic inhomogeneity of the material, the values do not exactly coincide; they will be denoted as J_{ca}^G J_{cb}^G J_{cc}^G J_{cd}^G. By tracing a profile perpendicular to the junction at the position of any pair of peaks (Figure 6.7, profile 4), it can be observed that the profile presents a minima which coincides with the junction position. Once the junction has been located, a profile along it can be traced (Figure 6.7, profile 2). The profile presents two peaks, corresponding to the inter-granular current density values, J_c^{GB}. Again, since the values at the two maximum do not exactly coincide, two J_c^{GB} values must be considered: J_{cf}^{GB} and J_{cg}^{GB}.

Due to the inhomogeneity of the samples, two J_c^{GB}/J_c^G ratios are obtained. The critical current density at the joint is compared with the lowest one of the two J_c^G values situated at each side of the weld. That is, for each sample, the J_{cf}^{GB} will be compared to the minimum of (J_{ca}^G, J_{cc}^G), and J_{cg}^{GB} to the minimum of (J_{cb}^G, J_{cd}^G). This estimation is justified by the fact that the critical current density at the joint obtained from the weld process can only be similar or lower than the smallest intra-grain critical current density of the YBCO monoliths to be joined.
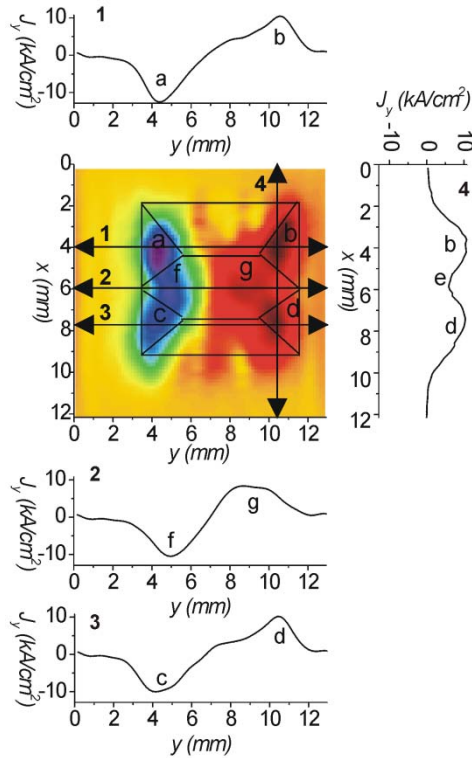
FIGURE 6.7 SCHEMATIC DIAGRAMS SUMMARIZING THE METHOD FOR THE DETERMINATION OF THE J_c^{GB} AND J_c^G FROM THE $J_y(x,y)$ MAP. J_c^G IS DETERMINED FROM THE PEAKS A AND B, IN PROFILE NUMBER **1**, AND FROM PEAKS C AND D IN PROFILE NUMBER **3**. THE POSITION OF THE WELD, WHICH IS MARKED AS E, IS FOUND FROM PROFILE **4**. THE J_c^{GB} VALUE IS DETERMINED FROM F AND G IN THE PROFILE ON TOP OF THE JOINT, REPRESENTED IN PROFILE **2**.

The case of a welded sample exhibiting a J_c^{GB}/J_c^G close to 1, the analysis has to be carried out differently, since the J_y map will present another shape. In that case, the four triangular zones merge into two.

In Figure 6.8, the case of a weld with high figure of merit has been presented. If two profiles are traced perpendicularly to the junction, it can be observed that the values of the current density at the junction position are comparable to those present in the rest of the material. On the left-hand site of the map, the profile shows its maximum value exactly on the junction.

If the J_c^{GB}/J_c^G ratio is calculated for the values obtained at the right-hand side of the map, that is $J_c^{GB}=14kA\cdot cm^{-2}$ and $J_c^{G\ min}=15kA\cdot cm^{-2}$, a value of 0.93 is obtained. In contrast, if the ratio is calculated at the left-hand side of the map, since the profile exhibits no local minimum, the J_c^{GB}/J_c^G ratio must be assumed to be one.
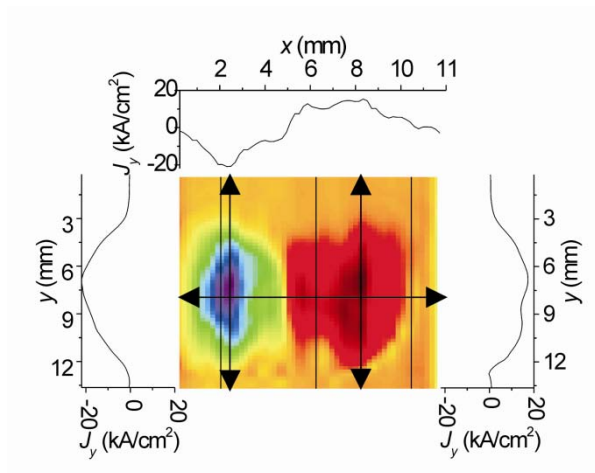
FIGURE 6.8 $J_y(x,y)$ MAP FOR A WELD EXHIBITING J_c^{GB}/J_c^G CLOSE TO **1.**

6.3.6 Global evaluation: Integration method

The values obtained by using the method described in the former section only provide information about the maximum values present in the $J_c(x,y)$ distribution. However, it could be interesting to also obtain the J_c^{GB}/J_c^G figure of merit, by considering a more global evaluation of the $J_c(x,y)$ maps. This evaluation is justified if one pretends to obtain values that would be comparable to those obtained from methods that intrinsically perform a more global evaluation of the electrical response of a superconducting material, such as transport measurements. Moreover, the use of the maxima method implies the risk of choosing a value that might not be representative to the sample reality.

For that reason, a complementary method for evaluating the $J_c(x,y)$ maps has been developed. Two profiles are considered in that case. The first is obtained from the $J_x(x,y)$ component and it is used to extract the J_c^G value. The $J_x(x,y)$ is integrated along the profile from the sample edge until the sign of $J_x(x,y)$ is changed, thus considering all the current that flows at the outmost part of the sample. The result of that integral is then divided by the distance, thus obtaining the desired mean J_c^G value.

The J_c^{GB} is obtained by profiling $J_y(x,y)$ along the weld position. That profile is integrated from the sample edge to the point where the $J_y(x,y)$ changes its sign.

On Table 6.1 a comparison of the results obtained on several samples is presented. As a general characteristic, the J_c values obtained from the integration method are lower. This fact is expected, since the integration method is considering a wider zone of the sample than on the method of the maximum value.

However, if the J_c^{GB}/J_c^G figure of merit obtained from the integration method is compared to that obtained from the maxima method, no clear tendency is observed. If the observations on the microstructure are considered, followed by a careful inspection of the magnetization maps, it can be observed that the samples used exhibit some grade of inhomogeneity on both properties.

a)
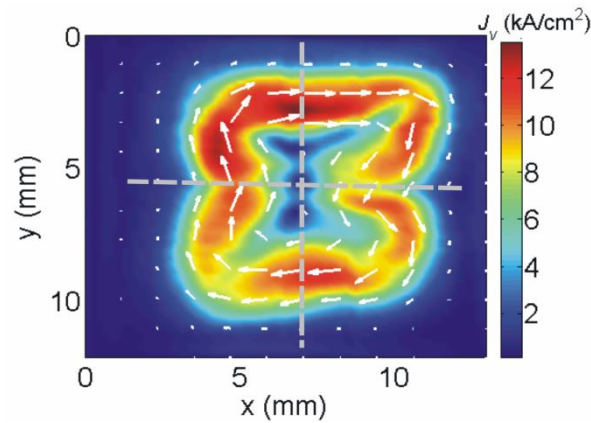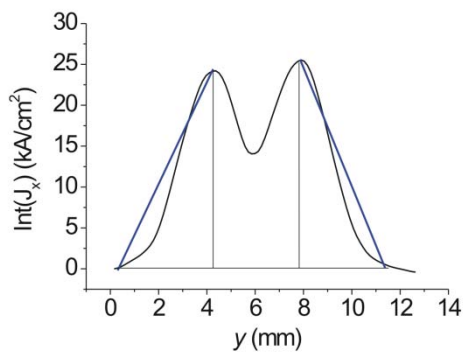
b)   c)
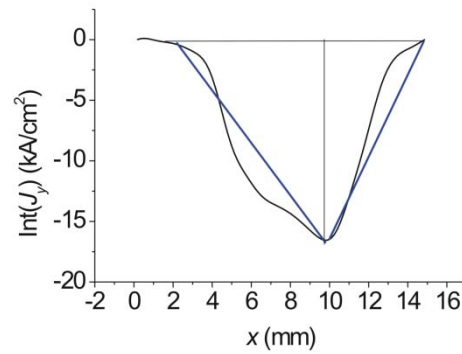
FIGURE 6.2 (A) CRITICAL CURRENT DENSITY MAP WHERE THE PROFILES USED FOR THE INTRA- AND INTER-GRANULAR CRITICAL CURRENT DENSITY DETERMINATION ARE INDICATED. (B) INTEGRATION OF THE J_x COMPONENT ALONG THE PROFILE (C) INTEGRATION OF THE J_y COMPONENT ALONG THE PROFILE

Despite that in the the integration method the values are closer to those that would be obtained from other macroscopic measurement methods, the figure of merit inferred from the integration might might lead to wrong conclusions about the weld performance. The case of Sample 15 (6.95° of misorientation) is an illustrative example: The J_c^{GB}/J_c^{G} figure of merit obtained from the maxima method is of 63%, whereas the figure of merit for the integration method is of 103%. If the J_c^{G} values are compared, the integration value is of 9245 A/cm^2, approximately the half of the 18759 A/cm^2 that are obtained from the maxima value. The difference between the J_c^{GB} is not so important: 9496 A/cm^2 from the integration case, in front of the 12219 A/cm^2 from the maxima method.

Therefore, maxima method is more suitable for the evaluation of the weld superconducting performance; even though the first impression is that the values obtained are not representative to the sample characteristics. Precisely due to the fact that the maxima method chooses the best value of the critical current density, it automatically rejects the effects caused by inhomogeneities in the sample under study. However, the integration method is still useful if the absolute values of the material as a whole have to be compared to those obtained from

other measurement techniques, since it compensates the over-evaluation effect of the maxima method.

Sample	Misorientation (deg)	J_c^G (kA/cm^2) Maxima	J_c^{GB} (kA/cm^2) Maxima	J_c^G (kA/cm^2) Integration	J_c^{GB} (kA/cm^2) Integration	J_c^{GB}/J_c^G Maxima	J_c^{GB}/J_c^G Integration
Sample1	14 ± 1	10.2 ± 0.1	6.0 ± 0.1	6.0 ± 0.1	4.3 ± 0.1	59%	71%
Sample2	6 ± 1	9.5 ± 0.1	5.5 ± 0.1	4.2 ± 0.1	3.2 ± 0.1	57%	74%
Sample3	4 ± 1	9.1 ± 0.1	6.1 ± 0.1	6.1 ± 0.1	4.4 ± 0.1	66%	72%
Sample4	24 ± 1	10.0 ± 0.1	6.6 ± 0.1	5.1 ± 0.1	3.2 ± 0.1	66%	62%
Sample5	8 ± 1	15.7 ± 0.1	9.4 ± 0.1	8.5 ± 0.1	3.4 ± 0.1	60%	40%
Sample6	1 ± 1	13.5 ± 0.1	9.8 ± 0.1	6.5 ± 0.1	5.4 ± 0.1	73%	83%
Sample7	4 ± 1	14.2 ± 0.1	13.6 ± 0.1	8.3 ± 0.1	8.8 ± 0.1	96%	106%
Sample8	5 ± 1	17.0 ± 0.1	8.7 ± 0.1	8.8 ± 0.1	5.6 ± 0.1	52%	64%
Sample9	6 ± 1	12.3 ± 0.1	10.0 ± 0.1	6.1 ± 0.1	5.5 ± 0.1	81%	90%
Sample10	11 ± 1	19.5 ± 0.1	10.0 ± 0.1	9.7 ± 0.1	4.9 ± 0.1	52%	50%
Sample11	11 ± 1	11.4 ± 0.1	6.9 ± 0.1	5.5 ± 0.1	2.5 ± 0.1	60%	46%
Sample12	16 ± 1	12.3 ± 0.1	7.8 ± 0.1	6.1 ± 0.1	4.3 ± 0.1	64%	71%
Sample13	14 ± 1	9.0 ± 0.1	7.9 ± 0.1	4.2 ± 0.1	3.5 ± 0.1	88%	84%
Sample14	4 ± 1	11.2 ± 0.1	8.1 ± 0.1	7.8 ± 0.1	5.8 ± 0.1	72%	75%
Sample15	7 ± 1	18.8 ± 0.1	12.2 ± 0.1	9.2 ± 0.1	9.5 ± 0.1	65%	103%
Sample16	14 ± 1	11.0 ± 0.1	7.6 ± 0.1	5.7 ± 0.1	3.0 ± 0.1	69%	52%
Sample17	13 ± 1	14.6 ± 0.1	7.9 ± 0.1	7.3 ± 0.1	3.5 ± 0.1	54%	49%
Sample18	24 ± 1	15.6 ± 0.1	9.8 ± 0.1	14.0 ± 0.1	10.5 ± 0.1	63%	75%

TABLE 6.1 COMPARISON OF THE VALUES OBTAINED FROM THE TWO DETERMINATION METHODS: MAXIMA AND INTEGRATION, TOGETHER WITH THEIR ASSOCIATED FIGURE OF MERIT

6.4 WORK 8: Vortex pinning regimes in YBa$_2$Cu$_3$O$_{7-x}$ bulk boundaries investigated by quantitative magnetic Hall microscopy

A proper study of the field dependence of the J_c^{GB} and the J_c^G was necessary in order to understand the weak dependence of the J_c^{GB}/J_c^G figure of merit on the misorientation angle. If potential industrial applications are taken into consideration, a more thorough knowledge of the behavior of the superconducting properties of the welds under a non-null magnetic field is required.

For a bearing that would be used for a flywheel energy storage system requires the use of relatively low magnetic field $\mu_0H\sim0.3$T, whereas motors would imply the use of higher magnetic fields $\mu_0H\sim0.6$T (medium power) or $\mu_0H>0.8$T (high power). As it will be later explained, different magnitudes of magnetic field potentially imply that different pinning regimes are present in the material and constrain the choice of the most appropriate weld misorientation.

6.4.1 Previous knowledge on thin films
Palau (56) developed an analytic method of the critical current density in YBCO coated conductors as a function of the applied field in order to foresee the flux pinning regimes. An identical analysis was performed on the welded samples using the same analysis tools.

In summary, the J_c^{GB} and the J_c^G of coated conductors was studied as a function of the magnetic field. The most relevant results of this study are explained below:

For the case of the J_c^G, three different dependencies were found if the $J_c(H)$ was plotted in logarithmic scale. For low fields, J_c^G exhibits a quasi-flat dependence. When the applied magnetic field is higher than an H_{cross} value the tendency changes to follow a power-law. If the magnetic field is further increased, when a H_{joint} value is overtaken, a stronger dependence is now followed.

J_c^{GB} also exhibited a similar behavior with the same three different regions: A quasi-plateau for $H < H_{cross}$, a power-law for $H > H_{cross}$ and $H < H_{joint}$ and a more abrupt dependence for $H > H_{joint}$.

For both cases, the existence of the H_{cross} and H_{joint} threshold values marked the border between three different vortex motion behaviors:

Zone 1: For the case of the grain, the most important pinning force for each vortex is the interaction of itself to the several grain defects. Vortex-vortex interactions are less important in that zone. For the case of the grain boundary, the motion of the Abrikosov-Josephson vortices present in the grain boundary is governed by the interactions between them and the strongly pinned Abrikosov vortices present at the adjacent grains.

Zone 2: As the field is increased, the pinning force to defects is overcome by the motion energy, and a more collective vortex-vortex interaction is promoted at the grains. Whereas, at the grain boundary, the Abrikosov-Josephson vortices interact less with the vortices present at the grains, so now the most important pinning force is the one with the defects at the grain boundary.

Zone 3: Finally, when H overcomes the H_{joint}, both Abrikosov and Abrikosov-Josephson vortices freely move, provoking the join of the J_c^{GB} and J_c^G values and its fast decay when the magnetic field is increased.

6.4.2   Measurement protocol and discussion

A set of welded tiles with several misorientations ranging from 0° to 30° were chosen for this study. Each one, was cooled down to 77K in zero field condition and, by using Hall probe microscopy setup previously introduced, local magnetization maps of each weld were obtained at different applied fields.

For each $M(x,y)$ map the $J_c(x,y)$ map was obtained by using the Caragol software package and the Bean Model based analytic tool introduced above was applied. This allowed obtaining the J_c^{GB} and J_c^G values as a function of the applied field.

The weld behavior is analogous to the case of thin film grain boundary: Flat dependence for $H < H_{cross}$, power-law for $H_{cross} < H < H_{joint}$ and a severe depression of the J_c^{GB} for $H > H_{joint}$. In consequence, a similar vortex motion is expected to take place compared to that present in thin films.

The situation is different for the grain case, since there is no clear transition between the three regimes observed for the thin-film case. A more smeared transition between a quasi-flat dependence to a faster decay of the J_c^G is observed. More in detail, the cause of this behavior can be modeled as softer transition at H_{cross}, followed by a higher dependence in the power-law and a less concrete value of the H_{joint}.

Despite this difference in the pinning regimes at the grain between the coated conductor and bulk case, the pinning regimes at the grain boundary/weld would be intrinsic to the grain boundary local characteristics and independent to the grain characteristics, although some differences with the power law α parameter are observed, that could be explained with the fact that the welds exhibit a meandering shape instead of an ideal 1D geometrical disposition.

It has to be considered that the starting material has an intrinsic inhomogeneous quality regarding its superconducting properties. This fact was taken into consideration and the correlation between J_c^G and J_c^{GB} was studied for several welded samples with a [001]-tilt misorientation of 11 deg and compared to similar cases of artificial bulk grain boundaries. The J_c^{GB}/J_c^G figure of merit for all the included cases were determined to have a value of around 0.598, proving that the final value of the J_c^{GB} is strongly determined by the value of J_c^G.

The correlation between J_c^{GB} and J_c^G was further investigated by comparing two welds with the same misorientation angle, but with different starting YBCO grain characteristics. The different grain characteristics are caused by different growth techniques between them. In particular, one of the compared starting YBCO grains has particle inclusions at the nanometer scale and, thus, an enhancement of the J_c^G was expected and confirmed. $J_c^{GB}(H)$ exhibited the sample behavior, defining the same three pinning regimes with the H_{cross} and H_{joint} values similar, but not identical. The J_c^{GB} absolute values for the modified YBCO growth process were higher than the YBCO grown from Nexans and correlated with the enhancement of the J_c^G value, thus reinforcing the hypothesis of the J_c^{GB} and J_c^G correlation for a given misorientation angle.

6.5 WORK 9: Effective silver assisted welding of YBCO blocks: mechanical versus electrical properties

The potential applications of this welding method include the use of the joined YBCO tiles under the presence of high magnetic fields and/or low temperatures. It is expected that a considerable amount of forces would be present in the material.

In particular, the thermal cycles expected when the device would be cooled down to cryogenic temperatures and, eventually heated up to room temperature would introduce stress in the material due to the thermal expansion. For the case of the application of large magnetic fields, torque forces are expected to be present.

For this reason the mechanical properties of a chosen set of samples with several characteristics was measured the using nano-indentation technique. Precisely, the Young modulus and nano-hardness was studied, by comparing the obtained values between those obtained in a position far away from the weld zone and those obtained at the weld zone.

Several cases were considered: A successfully welded sample with no misorientation, one with a low quality weld zone under the scope of its microstructural characteristics, and one with a 14 deg [001]-tilt misorientation.

For each case, a nano-indentation scan across the weld was performed. The scan length spanned for 2 cm symmetrically respect to the weld position with a separation of 50μm between imprints. The resulting imprints were observed with a field emission electron microscope. From the dimensions and shape of the imprint, the hardness was determined.

As expected, the high quality welded sample with no misorientation exhibited no difference between the weld and the rest of the scanned zone, thus giving a correlation with the observed microstructure and J_c^{GB}/J_c^G figure of merit.

The two welded samples with a 14 deg misorientation exhibited weaker hardness at the weld zone compared to that present at the rest of the scan zone. This result also correlates with the lower J_c^{GB}/J_c^G figure of merit and local microstructural defects such as cracks present in those samples.

The fourth considered case, consisting of a low quality weld with no misorientation, also gives a good correlation with the previous electrical and microstructural characterizations.

If the J_c^{GB}/J_c^G figure of merit is compared with the ratio between the hardness at the grain and grain boundary, $H(GB)/H(G)$, a clearly linear correlation is observed, thus indicating the close relationship between the electrical and mechanical properties.

6.6   Summary

The development of a suitable magnetic characterization setup was needed, in order to properly obtain the required information from the magnetic measurements. For that purpose, a Hall probe based magnetic imaging system was built. It allowed obtaining the local magnetization of the sample under study as a function of the Hall probe position.

In parallel, a software package called "Caragol" was developed by M. Carrera and J. Amorós and its purpose was the obtention of the critical current density distribution of the sample from the magnetization maps. Although the software is available online a specialized version, that outputted higher resolution current density maps, was used.

Since the obtained critical current density maps exhibited a very complex distribution, it was necessary to, first, model the problem of the welded with a suitable theoretical model. The chosen model was the case of two single crystals joined with a grain boundary. Simulation software was specially developed for simulating the critical current density distribution.

The simulated current maps, together with applying the Bean model to the case of a bi-crystal were of a great help for the simultaneous obtention of the inter- and intra-granular critical current density components from a given $J_c(x,y)$ map. Two distinct methodologies were developed: A local evaluation of the $J_c(x,y)$ maps and a more global evaluation, that considered a wider zone of the $J_c(x,y)$ maps for the determination of the J_c^{GB} and J_c^G values.

Once the analytic methodology was properly established, it was used as a quality test for evaluating the successfulness of the weld formation for the scenario of the thermal process optimization and, later, for studying the influence of the introduction of a crystallographic misorientation between the joined tiles.

The dependence of the J_c^{GB}/J_c^{G} figure of merit with the crystallographic misorientation was found to be less important than expected, especially if that dependence was compared to that exhibited by a thin film. A possible hypothesis for this difference could be a particular vortex pinning regime, not present in the case of a thin film. For that purpose, field dependent Hall image measurements were carried out and, from the dependence of the extracted J_c^{G} and J_c^{GB} values with the applied magnetic field, the vortex pinning regimes were predicted. In spite of the difference of the grain pinning regimes observed between coated conductor and bulk cases, the grain boundary pinning regimes were found to be similar. J_c^{GB} and J_c^{G} are strongly correlated for a misorientation of a given angle, thus indicating that the depression of the superconducting properties at the grain boundary is intrinsic to the fact of its existence.

Finally, since the microstructural analysis on weld samples with misorientation revealed a high probability of crack development at the weld position, the mechanical properties of the welds were investigated. For the case where no misorientation was introduced and the weld was successfully formed, the nano-indentation measurements carried out did not reveal any difference between the hardness at the weld position and at the grain position. The scenario changes for low quality non-misoriented welds, where a depression of the hardness was found. Similar depression was also discovered when a misorientation weld case was considered. In summary, the J_c^{GB}/J_c^{G} exhibited a high correlation with the hardness weld to grain ratio, thus revealing a close relationship between the electrical and mechanical properties.

WORK 5:

"In-field magnetic Hall probe microscopy studies of $YBa_2Cu_3O_7$ based superconductors"

E. Bartolomé, X. Granados, B. Bozzo, S. Iliescu, T. Puig, X. Obradors

Journal of Physics and Chemistry of Solids **67** (2006) 403–406

DOI: 10.1016/j.jpcs.2005.10.146

WORK 6:

"Simulation of dc magnetic effects due to geometrically defined grain boundaries in type-II superconductors"

E. Bartolomé, X. Granados, B. Bozzo, C. Navau, T. Puig, X. Obradors

Physica C **468** (2008) 492–497

DOI: 10.1016/j.physc.2008.02.003

WORK 7:

"Determination of the inter- and intra-granular critical currents in superconducting $YBa_2Cu_3O_7$ welds"

B. Bozzo, S. Iliescu, E. Bartolomé, A. Palau, X. Granados, T. Puig, X. Obradors, J. Amorós and M. Carrera

Supercond. Sci. Technol. **18** (2005) 1227–1232

DOI: 10.1088/0953-2048/18/9/015

WORK 8:

"Vortex pinning regimes in $YBa_2Cu_3O_{7-x}$ bulk boundaries investigated by quantitative magnetic Hall microscopy"

E. Bartolomé, B. Bozzo, X. Granados, F. Sandiumenge, T. Puig and X. Obradors

Supercond. Sci. Technol. **21** (2008) 125002

DOI: 10.1088/0953-2048/21/12/125002

WORK 9:

"Effective silver-assisted welding of YBCO blocks: mechanical versus electrical properties"

E. Bartolomé, J. J. Roa, B. Bozzo, M. Segarra and X. Granados

Chapter 7.   Conclusions

Seed based crystal growth techniques are based on promoting the heterogeneous solidification from a single point at the seed position. That growth occurs when slowly cooling down the material and, when temperature is low enough, other nucleation centers compete with the seed nucleation center.

For the particular case of the Top Seeded Melt Growth method for producing YBCO, that nucleation competition implies a limitation on the maximum size of the pellets that can be fabricated and, since the trapped field on an YBCO pellet is size dependent, it has been necessary to investigate methods for overcoming this limitation.

At the starting point of the work presented in this Thesis, a silver assisted welding method was being developed and the final optimization and the solving of the liquid loss problem were still pending.

A better understanding of the mechanisms that make the weld formation was also necessary. For that purpose, as a complementary tool to the microstructure observations, a special furnace, equipped with a video-camera was built. The videos recorded during the thermal treatment for several samples revealed:

- The existence of a silver rich liquid, exhibiting a very low viscosity that was leaking out from the weld position.
- The appearance of a second liquid at the sample holder indicated that, during the thermal treatment, a considerable amount of molten material was lost.

The liquid loss was considered a potential problem for the proper weld formation. In fact, the microstructure analysis on the weld revealed a high chance that unreacted phases at the weld position would form. For that reason, the relationship to the growth parameters (T_{max} and

silver mass) was studied, revealing no clear correlation, thus indicating that a more complex phenomena was involved in that loss of liquid.

The use of alumina as a sample holder was postulated to have an impact on the liquid loss, since its porous nature would promote that loss. That promotion was probed when an MgO plate was introduced between the alumina holder and the sample, since all the samples produced with this modification exhibited no mass loss and that source of irreproducibility was eliminated.

Since the orthorhombic and superconducting Y-123 phase depends on the oxygen content. A correct choice of the oxygenation time is required since either an under-doping or an over-doping depresses the superconducting properties. For a bulk YBCO with no defects, the predicted oxygenation times from diffusion equations are much longer than those found from experimental investigation. Moreover, it was postulated that the crack formation during the oxygenation would play a relevant role in shortening that oxygenation time. With the use of thermogravimetric techniques, the confirmation of the role of the crack formation on the oxygenation time was quested. That study indicated that:

- If the starting material has never been oxygenated, as the orthorhombic phase is being formed, cracks are developed.
- At the same time, the stress generated between the zone where cracks are formed and the virgin zone promote a further crack formation.
- Crack formation increased the contact surface to the oxygen atmosphere, thus making this time reduction possible.
- The case of the second and third oxygenation represent the scenario of the starting material with cracks already present and, in those cases, the thermogravimetric curve exhibited a completely different shape, revealing shorter oxygenation times than in the first oxygenation curve. This fact further confirmed the role of cracks in this time reduction.

However, if the use of bulk YBCO pellets is thought in terms of technological applications, many of them would require the introduction of a certain crystallographic misorientation between the joined tiles. This applies to the case of motor bearings, where a [100]-tilt type misorientation would be required, whereas for the case of a flywheel component for energy storage it would require a [001]-tilt misorientation, for instance.

For that reason, the welding technique under study was extended to include the case of the introduction of some misorientation. For simplicity, the [001]-tilt case was considered and the angular dependence on the microstructure and superconducting properties was studied.

The study of the microstructure of the welds has been a crucial tool for many purposes:

- A basic characterization of the microstructure of the weld, seeking for unreacted phases or voids was used as a feedback for the high temperature thermal treatment tailoring.

84

- A thorough study aiming to a better understanding of the weld formation mechanisms. The crack formation, Y-211 particle distribution, intrinsic misorientations, real misorientation were the studied items.

That microstructural characterization study revealed that:

- Liquid loss is a source of formation of voids and unreacted phases.
- Y-211 particle distribution at the weld position is modified with a clear decrease of the presence of the smallest particles. With the YBCO-Ag phase diagram in consideration, the reason for this modification would by a deficiency of Y during the thermal process.
- Welds have been successfully formed, however, during the oxygenation process, the chance of crack formation at the weld position increases as the misorientation angle increases. This fact would impose a limit on the maximum misorientation that should be considered in potential technological applications.
- The presence of intrinsic mosaicity on the starting material implies that no pure [001]-tilt misorientation exists and it is intrinsic to the material, due to its existence in a large zone far from the weld position. The thermal process does not introduce a modification on this sub-grain structure, indicating a highly localized molten zone.
- If unreacted phases and cracks exist at the weld position, they are strongly localized. A modification of the weld plane to a plane that it is not a cleavage plane of the Y-123 system lowers the presence of cracks and modifies the structure of the unreacted phases in the case that they exist.

It has to be emphasized that achieving a good microstructure is not enough to be successful in the welding method. It should not be forgotten that most of the potential applications of bulk superconductors rely on their capacity of trapping magnetic field and act as extremely powerful permanent magnets. The main reason for developing the welding techniques is to enhance the global magnetic performance of the resulting joined system. For that reason, the magnetic and electric properties of the welded samples were investigated.

With the purpose of investigating the homogeneity of the magnetic and electric properties, a setup that allowed obtaining local magnetization maps at the sample surface was built. With the help of specialized software, the critical current distribution maps could be obtained from those magnetization maps.

The critical current density maps exhibited a very complex distribution that required the development of the appropriate analysis tools with the obtention of the intra- and inter-granular critical current densities in aim.

In order to simulate the critical current distribution for the case of welded samples, a software piece called "Trazacorrientes" was developed. With no assumption about the geometrical characteristics of the sample to be simulated, the software was filling the sample space with currents with the only constrain of maximizing the surface enclosed by the current loop. The software was tested with a large number of situations and the simulated patterns were contrasted with real samples, showing a good agreement.

The simulation for the weld case, with the help of Bean model, allowed us to distinguish key zones on the critical current distribution, where the extraction of the inter- and intra-granular critical current densities became more trivial.

However, Trazacorrientes and the Bean model rely on the following two assumptions that are not accomplished in a real situation: J_c is independent of the magnetic field and the sample is infinitely long. Moreover, in a real situation, the presence of some grade of inhomogeneity in the starting magnetization maps, not related to the weld, had to be considered.

With the knowledge of the results obtained from Trazacorrientes, the intra- and inter-granular critical current densities for a real welded sample were determined using two methods:

- Local method or maxima method.
- Global method or integration method.

In general, global method values would be closer to those obtained from other techniques such as electrical transport. However, a global evaluation intrinsically includes inhomogeneities present in the sample that, in some cases, lead to wrong conclusions about the weld performance. In consequence:

- Maxima method is the preferred method if the J_c^{GB}/J_c^G figure of merit has to be determined, since it intrinsically rejects the inhomogeneities that might be present in the material that diminish the superconducting properties.
- Integration method would be preferable if more macroscopic critical current density values needs to be provided.
- The angular dependence of the J_c^{GB}/J_c^G figure of merit was not as strong as expected, especially if it is compared to that obtained in thin films. It was later observed that this weaker dependence is a common feature for grain boundaries in bulk YBCO. It was postulated that different pinning mechanisms between the bulk and the thin film case would be present.

With the study of the magnetic field dependence of J_c^G and J_c^{GB}, the pinning regimes were identified and compared to the case of a coated conductor. It was observed that:

- The characteristics of the Grain boundary pinning are intrinsic and independent of the grain characteristics, although slight differences on the power-law have been determined.
- J_c^{GB}/J_c^G figure of merit, for a given misorientation angle, is independent of the grain characteristics.

Finally, the observations on the microstructure and the magnetic/electric properties indicate a potential correlation, especially on the chance of crack formation at the weld position. Higher misorientation angles would lead to higher amount of stress at the weld position, thus degrading the mechanical properties.

For that purpose, the mechanical properties were measured using nano-indentation techniques. With the cases considered (high quality non-misoriented weld, low quality-misoriented weld and mid-range misorientation) it was found that:

- High quality non-misoriented welds exhibit no change in the hardness if they are compared with the values away from the weld zone.
- Low quality non-disoriented weld and mid-range misoriented welds both exhibited a depression on the hardness value.
- There exists a high correlation between the H(GB)/H(G) hardness ratio and the J_c^{GB}/J_c^G figure of merit. This indicates that the mechanical, microstructural and superconducting properties have a very close relationship.

In summary, the welding technique was found to be a valid solution for enhancing the limitations in size and shape of the YBCO growth methods, thus making possible to produce larger YBCO pieces with specific shapes and, thus, enhancing the magnetic properties. Even though the introduction of crystallographic misorientations degrades somehow the superconducting properties of the weld, due to the fact that an artificial grain boundary is introduced, a careful choice of the shape of the superconducting element can mitigate that effect.

As a final remark, we should remind that nowadays the most promising research line in superconductivity relies on the use of thin films with the aim to produce superconducting wires based on the epitaxial growth of the YBCO on top of a metallic substrate with the appropriate mechanical properties. The scenario where several superconducting wires should be joined, while preserving the superconducting properties at the join appears also very attractive. In consequence, the knowledge acquired from this work could potentially be used to adapt the weld methodology to the particular case of thin films.

Chapter 8. Bibliography

1. J. R. Waldram, in *Superconductivity of Metals and Cuprates*. (Institute of Physics Publishing, 1996), chap. 2.
2. J. R. Waldram, in *Superconductivity of Metals and Cuprates*. (Institute of Physics Publishing, 1996), chap. 4.
3. J. R. Waldram, *Superconductivity of Metals and Cuprates*. (Institute of Physics Publishing, 1996).
4. M. Murakami, in *Melt Processed High-Temperature Superconductors*. (World Scientific, 1992), chap. 6, pp. 101-132.
5. C. P. Bean, Magnetization of Hard Superconductors. *Physical Review Letters* **8**, 250-& (1962).
6. Y. B. Kim, C. F. Hempstead, A. R. Strnad, Critical Persistent Currents in Hard Superconductors. *Physical Review Letters* **9**, 306-& (1962).
7. J. Silcox, R. W. Rollins, Hysteresis in Hard Superconductors. *Applied Physics Letters* **2**, 231-233 (1963).
8. K. Yasukochi, T. Ogasawara, N. Usui, Magnetic Behavior + Effect of Transport Current on It in Superconducting Nb-Zr Wire. *Journal of the Physical Society of Japan* **19**, 1649-& (1964).
9. W. A. Fietz, J. Silcox, M. R. Beasley, W. W. Webb, Magnetization of Superconduction Nb-25(Zr Wire. *Physical Review A-General Physics* **136**, A335-& (1964).
10. S. Iliescu, *Superconducting Joints of Melt-Textured YBa2Cu3O7-d monoliths: Preparation, Microstructure and Critical Currents*, Universitat Autònoma de Barcelona, (2004).
11. J. G. Bednorz, K. A. Muller, Possible High-Tc Superconductivity in the Ba-La-Cu-O System. *Zeitschrift fur Physik B-Condensed Matter* **64**, 189-193 (1986).
12. M. K. Wu *et al.*, Superconductivity at 93-K in A New Mixed-Phase Y-Ba-Cu-O Compound System at Ambient Pressure. *Physical Review Letters* **58**, 908-910 (1987).
13. D. C. Larbalestier *et al.*, Weak Links and the Poor Transport Critical Currents of the 123 Compounds. *Physica C* **153**, 1580-1585 (1988).
14. D. Larbalestier, Critical Currents and Magnet Applications of High-Tc Superconductors. *Physics Today* **44**, 74-82 (1991).
15. D. Dimos, P. Chaudhari, J. Mannhart, Superconducting Transport-Properties of Grain-Boundaries in Yba2Cu3O7 Bicrystals. *Physical Review B* **41**, 4038-4049 (1990).
16. M. Murakami, Processing of Bulk Ybacuo. *Superconductor Science & Technology* **5**, 185-203 (1992).
17. S. Jin *et al.*, High critical currents in Y-Ba-Cu-O superconductors. *Appl. Phys. Lett* **52**, 2074-2076 (1998).

18. E. Mendoza, *Obtenció i caracterització de ceràmiques texturades de YBCO per l'aplicació de limitació de corrent*, Universitat Autònoma de Barcelona, (2002).

19. X. H. Zeng, X. Yao, J. Hu, Y. L. Zhang, G. Li, Study on the NdBCO LPE thick film seed for the melt-textured growth of YBCO and (Y,Sm)BCO. *Physica C: Superconductivity* **412–414, Part 1**, 103-106 (2004).

20. C. Cai, H. Fujimoto, Effects of Nd123/MgO thin film and MgO single-crystal seeds in isothermal solidification of YBaCuO/Ag. *Journal of Materials Research* **15**, 1742-1748 (2000).

21. N. H. Babu, M. Kambara, P. J. Smith, D. A. Cardwell, Y. Shi, Fabrication of large single-grain Y-Ba-Cu-O through infiltration and seeded growth processing. *Journal of Materials Research* **15**, 1235-1238 (2000).

22. K. Iida, N. H. Babu, Y. Shi, D. A. Cardwell, Seeded infiltration and growth of large, single domain Y-Ba-Cu-O bulk superconductors with very high critical current densities. *Superconductor Science & Technology* **18**, 1421-1427 (2005).

23. E. S. Reddy, N. H. Babu, Y. Shi, D. A. Cardwell, G. J. Schmitz, Processing of large grain Y-123 superconductors with pre-defined porous structures. *Superconductor Science & Technology* **18**, S15-S18 (2005).

24. S. Meslin, K. Iida, N. H. Babu, D. A. Cardwell, J. G. Noudem, The effect of Y-211 precursor particle size on the microstructure and properties of Y–Ba–Cu–O bulk superconductors fabricated by seeded infiltration and growth. *Superconductor Science and Technology* **19**, 711 (2006).

25. L. H. Chen, H. Claus, A. P. Paulikas, H. Zheng, B. W. Veal, Joining of melt-textured YBCO: a direct contact method. *Superconductor Science & Technology* **15**, 672-674 (2002).

26. Y. A. Jee, C. J. Kim, T. H. Sung, G. W. Hong, Top-seeded melt growth of Y-Ba-Cu-O superconductor with multiseeding. *Superconductor Science & Technology* **13**, 195-201 (2000).

27. C. J. Kim *et al.*, Multiseeding with (100)/(100) grain junctions in top-seeded melt growth processed YBCO superconductors. *Physica C* **338**, 205-212 (2000).

28. K. Salama, V. Selvamanickam, Joining of High-Current Bulk Y-Ba-Cu-O Superconductors. *Applied Physics Letters* **60**, 898-900 (1992).

29. H. Walter *et al.*, Large intergranular critical currents in joined YBCO monoliths. *Europhysics Letters* **55**, 100-104 (2001).

30. J. G. Noudem, E. S. Reddy, M. Tarka, M. Noe, G. J. Schmitz, Melt-texture joining of YBa2Cu3Oy bulks. *Superconductor Science & Technology* **14**, 363-370 (2001).

31. J. Yoshioka *et al.*, Joining Y123 bulk superconductors using Yb-Ba-Cu-O and Er-Ba-Cu-O solders. *Superconductor Science & Technology* **15**, 712-716 (2002).

32. Y. Nakamura, K. Tachibana, H. Fujimoto, Dispersion of silver in the melt grown YBa2Cu3O6+x crystal. *Physica C* **306**, 259-270 (1998).

33. X. Obradors *et al.*, Chemical solution deposition: a path towards low cost coated conductors. *Superconductor Science & Technology* **17**, 1055-1064 (2004).

34. K. Kimura *et al.*, Development of REBCO Coated Conductors by TFA-MOD Method With High Properties in Magnetic Fields. *Ieee Transactions on Applied Superconductivity* **25**, (2015).

35. M. Lei *et al.*, Preparation of Coated Conductors With Fluorine-Free CSD Method. *Ieee Transactions on Applied Superconductivity* **25**, (2015).

36. D. Kenfaui, P.-F. Sibeud, E. Louradour, X. Chaud, J. G. Noudem, An Effective Approach for the Development of Reliable YBCO Bulk Cryomagnets with High Trapped Field Performances. *Advanced Functional Materials* **24**, 3996-4004 (2014).

37. R.-P. Sawh, R. Weinstein, K. Carpenter, D. Parks, K. Davey, Production run of 2 cm diameter YBCO trapped field magnets with surface field of 2 T at 77 K. *Superconductor Science & Technology* **26**, (2013).

38. S. P. K. Naik, N. D. Kumar, P. M. S. Raju, T. Rajasekharan, V. Seshubai, Effect of infiltration temperature on the properties of infiltration growth processed YBCO superconductor. *Physica C-Superconductivity and Its Applications* **487**, 72-76 (2013).

39. D. H. N. Dias *et al.*, Application of textured YBCO bulks with artificial holes for superconducting magnetic bearing. *Superconductor Science & Technology* **28**, (2015).

40. M. Sparing *et al.*, Superconducting Magnetic Bearing as Twist Element in Textile Machines. *Ieee Transactions on Applied Superconductivity* **25**, (2015).

41. T. Puig *et al.*, Self-seeded YBCO welding induced by Ag additives. *Physica C* **363**, 75-79 (2001).

42. C. Harnois, X. Chaud, I. Laffez, G. Desgardin, Joining of YBCO textured domains: a comparison between the multi-seeding and the welding techniques. *Physica C* **372**, 1103-1106 (2002).

43. S. Iliescu *et al.*, Melting of Ag-YBa$_2$Cu$_3$O$_7$ interfaces: the path to large area high critical current welds. *Superconductor Science & Technology* **18**, 168-172 (2004).

44. Y. Nakamura *et al.*, Phase relation in Y211-Y123-Ag system and morphology of silver in Y123 crystal. *Physica C-Superconductivity and Its Applications* **294**, 302-315 (1998).

45. P. Diko, G. Fuchs, G. Krabbes, Influence of silver addition on cracking in melt-grown YBCO. *Physica C* **363**, 60-66 (2001).

46. E. Mendoza *et al.*, Critical current enhancement in YBCO-Ag melt-textured composites: influence of microcrack density. *Physica C* **334**, 7-14 (2000).

47. Y. H. Shi, A. R. Dennis, D. A. Cardwell, A new seeding technique for the reliable fabrication of large, SmBCO single grains containing silver using top seeded melt growth. *Superconductor Science & Technology* **28**, (2015).

48. K. Konstantopoulou *et al.*, Mechanical characterization of GdBCO/Ag and YBCO single grains fabricated by top-seeded melt growth at 77 and 300 K. *Superconductor Science and Technology* **27**, 115011 (2014).

49. S. Iliescu, *Superconducting Joints of Melt-Textured YBa2Cu3O7-d monoliths: Preparation, Microstructure and Critical Currents, Chapter 8*, Universitat Autònoma de Barcelona, (2004).

50. J. Figueras, T. Puig, A. E. Carrillo, X. Obradors, In-plane Mg doping in YBa2Cu3O7: influence on the superconducting anisotropy. *Superconductor Science & Technology* **13**, 1067-1073 (2000).

51. L. Raffo, R. Caciuffo, D. Rinaldi, F. Licci, Effects of Mg Doping on the Superconducting Properties of Yba2Cu3O7-Delta and La1.85Sr0.15Cuo4 Systems. *Superconductor Science & Technology* **8**, 409-414 (1995).

52. J. Zeng, Y.-H. Zhou, H.-D. Yong, Fracture behaviors induced by electromagnetic force in a long cylindrical superconductor. *Journal of Applied Physics* **108**, (2010).

53. H.-D. Yong, Y.-H. Zhou, J. Zeng, Crack problem in a long cylindrical superconductor. *Journal of Applied Physics* **104**, (2008).

54. M. Carrera, J. Amorós, X. Obradors, J. Fontcuberta, A new method of computation of current distribution maps in bulk high-temperature superconductors: analysis and validation. *Superconductor Science & Technology* **16**, 1187-1194 (2003).

55. A. Palau, T. Puig, J. Gutierrez, X. Obradors, F. de la Cruz, Pinning regimes of grain boundary vortices in YBa2Cu3O7-x coated conductors. *Physical Review B* **73**, (2006).

56. A. Palau, *Critical currents and dissipation of grain boundary networks in coated conductors*, Universitat Autònoma de Barcelona, (2005).